

Optimization Of Transducers For Active Structural Acoustic Control
Of Complex Structures Using Numerical Techniques

by

Denny E. Davis II

Thesis submitted to Faculty of the
Virginia Polytechnic and State University

in partial fulfillment of the requirements for the degree of

Master of Science

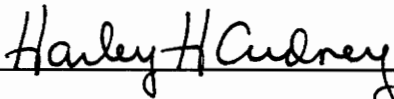
in

Mechanical Engineering

APPROVED:



Dr. Chris R. Fuller, Chairman



Dr. Harley H. Cudney



Dr. Alfred L. Wicks

April, 1995

Blacksburg, Virginia

C.2

LD
5655
V855
1975
D384
C.2

Optimization Of Transducers For Active Structural Acoustic Control Of Complex Structures Using Numerical Techniques

by

Denny E. Davis II

Committee Chairman: Chris R. Fuller

Mechanical Engineering

(ABSTRACT)

A general procedure for the optimization of control actuator forces and locations to minimize the total radiated sound power from complex structures has been developed. This optimization procedure interfaces finite and boundary element models with non-linear optimization techniques. The optimization procedure was used to perform parametric studies of Active Structural Acoustic Control (ASAC) on a simply supported plate with various discontinuities such as point mass, line mass, and spring mass systems. These system models were harmonically excited by an off resonance point force of 550 Hz and controlled by piezoceramic actuators. Although the excitation frequency is the same for each of the cases studied, the eigenproperties change with alteration of the physical parameters of the system. Therefore the excitation frequency for each case is effectively different, as is its response. This optimization procedure was very effective in reducing the total radiated sound power from these complex structures. The addition of a

second optimized actuator resulted in additional attenuation of varying extent, highly dependent on the discontinuity. The locations of the optimized actuators were also found to be very sensitive to the discontinuity. It was also observed that the optimal location of a single actuator changed very little with the addition of a second actuator. The accuracy of this sophisticated model was verified by comparing solutions from modal based analytical and assumed mode models for simple and complex structures. Some unique aspects of this procedure are that it requires a single implementation of the finite and boundary element solution, and that the finite element forced response solution is not required. Therefore, this ASAC actuator optimization procedure shows potential for application to any structure that can be accurately modeled with finite element software.

Acknowledgements

I would first like to thank my major professor Chris Fuller who directed my research, providing insight, and giving me the opportunity to work on this project.

I would also like to thank Robert Clark who got me up to speed with his work so that I could apply it to my project. Invaluable further guidance and direction was achieved because of the unselfish input of Ricardo Burdisso. Also ever present when things needed to be done in a hurry was Dawn Williams, willing to do whatever she could to make it happen.

I would also like to thank everyone in the group for their assistance and friendship both at work and away. Thank you Bertrand Brevart, Steve Lane, Julien Maillard, Tao Song, and Clark Smith. Special thanks to coworkers and friends who not only helped me at work but helped me forget work through racketball, snow skiing, water skiing, mountain biking, hiking, etc. Thank you Steve Booth, Jamie Carneal, Florence Deneufve, Gary Gibbs, D.J. Osborne, and Barry Robinson, Jerome Smith, and Pete Zinck.

I would also like to thank my Karate instructor, Ed Hampton, for making an enormous impact on my life and helping me develop the mentality I need to

achieve such goals in addition to overall perspective on life.

I must also thank Craig Rogers who through directing me in undergraduate research with Steve Stein got me interested in the pursuit of a graduate degree.

Most of all I must thank my mother for her undying source of support, encouragement, motivation, spirit, understanding, and love. I also thank my sister Sarah for friendship and hospitality, especially during those terrible ice storms when she provided Gary and I a place to eat and sleep. Thanks to my grandparents Kenneth Adams and Denvil Davis who also helped make it possible for me to pursue this degree.

Finally I acknowledge and thank the Office Of Naval Research (ONR) for their financial support of this project.

Table Of Contents

Chapter 1

Introduction	1
1.1 Noise Control	2
1.2 Active Structural Acoustic Control	5
1.3 Scope and Objective	10
1.4 Organization	11

Chapter 2

Analytical Model	13
2.1 Dynamic Response	13
2.2 Point Force Model	16
2.3 Piezoceramic Actuator Model	17
2.4 Total Structural Response	20
2.5 Acoustic Response	21
2.6 Objective Function	22

Chapter 3

Assumed Modes Method	28
3.1 Eigenvalue Formulation	28
3.2 Point Force Model	31

3.3 Piezoceramic Actuator Model	32
3.4 Total Structural Response	33
3.5 Acoustic Response	33
3.6 Objective Function	34

Chapter 4

Numerical Model	35
4.1 Finite Element Model	35
4.1.1 Point Force Model	40
4.1.2 Piezo Actuator Model	43
4.2 Boundary Element Model	49
4.2.1 Objective Function	53

Chapter 5

Control and Optimization Approach	58
5.1 Design Variables and Physical Constraints	58
5.2 Linear Quadratic Optimal Control Theory	61
5.3 Nonlinear Optimization	64
5.4 Review of IMSL Codes	66

Chapter 6

Model Verification	71
6.1 Simple Structure	72
6.2 Complex Structures	79
Chapter 7	
Point Mass Parametric Study	85
7.1 Simple Structure	86
7.2 Centered Point Mass	93
7.3 Off Center Point Mass	108
Chapter 8	
Line Mass Parametric Study	124
Chapter 9	
Spring Mass Parametric Study	140
9.1 Multiple Actuators and Robustness	154
Chapter 10	
Conclusions and Recommendations	156
Bibliography	159

List Of Figures

Figure 2.1: Plate Coordinate System	15
Figure 2.2: Schematic of PZT Actuator Pair	19
Figure 2.3: Objective Function Coordinate System	25
Figure 4.1A: Line Moment Piezo Model, B: Line Moment	45
Figure 4.2: Objective Function Field Points	55
Figure 4.3: Top View of Hemisphere	56
Figure 5.1: Schematic Of Plate Configured With A Single PZT	60
Figure 6.1: Directivity Patterns For Simple Structure Model Verification	76
Figure 6.2: Directivity Pattern For Simple Structure Modal Verification	77
Figure 6.3: Directivity Pattern For Simple Structure Numerical Model Verification	78
Figure 6.4: Directivity Patterns For Complex Structure Model Verification	84
Figure 7.1: Simple Structure Directivity Pattern	89
Figure 7.2: Control Actuator Locations For Simple Structure	90
Figure 7.3: Objective Function For 1 PZT	91
Figure 7.4: Objective Function For 2 PZTs	92
Figure 7.5: Deformed Modes With Center Mass	96
Figure 7.6: Directivity Pattern With 15% Center Mass	99
Figure 7.7: Directivity Pattern With 20% Center Mass	100
Figure 7.8: Directivity Pattern With 25% Center Mass	101

Figure 7.9: Control Actuator Locations With Center Mass	104
Figure 7.10: Objective Function For 1 PZT With 15% Center Mass	105
Figure 7.11: Objective Function For 1 PZT With 25% Center Mass	106
Figure 7.12: Objective Function For 2 PZTs With 15% Center Mass	107
Figure 7.13: Slightly Deformed Modes Shapes With Off Center Mass	110
Figure 7.14: Majorly Deformed Mode Shapes With Off Center Mass	111
Figure 7.15: Directivity Pattern With 15% Off Center Mass	114
Figure 7.16: Directivity Pattern With 20% Off Center Mass	115
Figure 7.17: Directivity Pattern With 25% Off Center Mass	116
Figure 7.18: Control Actuator Locations With Off Center Mass	117
Figure 7.19: Directivity Pattern For Sub-optimal Control With 25% Off Center Mass	121
Figure 7.20: Objective Function For 1 PZT With 20% Off Center Mass	122
Figure 7.21: Objective Function For 2 PZTs With 20% Off Center Mass	123
Figure 8.1: Deformed Mode Shapes With Line Mass	126
Figure 8.2: Directivity Pattern With 15% Line Mass	130
Figure 8.3: Directivity Pattern With 25% Line Mass	131
Figure 8.4: Directivity Pattern With 50% Line Mass	132
Figure 8.5: Directivity Pattern With 100% Line Mass	133
Figure 8.6: Control Actuator Locations With Line Mass	137
Figure 8.7: Objective Function For 1 PZT With 50 % Line Mass	138

Figure 8.8: Objective Function For 2 PZTs With 50 % Line Mass 139

Figure 9.1: Directivity Pattern For Below Resonance Model 146

Figure 9.2: Directivity Pattern For At Resonance Model 147

Figure 9.3: Directivity Pattern For Above Resonance Model 148

Figure 9.4: Control Actuator Locations With Spring Mass System 151

Figure 9.5: Objective Function For One PZT Below Resonance System . . . 152

Figure 9.6: Objective Function For One PZT Above Resonance System . . . 153

List Of Tables

Table 2.1: Steel Plate Material Properties	14
Table 2.2: PZT Material Properties	18
Table 2.3: Objective Function Coordinates	26
Table 3.1: Modal Indices	29
Table 4.1: Field Point Coordinates	57
Table 6.1: Natural Frequencies	74
Table 6.2: Natural Frequencies With Center Mass	81
Table 7.1: Simple Structure Solutions	88
Table 7.2: Natural Frequencies With Center Mass	94
Table 7.3: Radiation Efficiencies With Center Mass	97
Table 7.4: Sound Power And Attenuation With Centered Mass	98
Table 7.5: Natural Frequencies With Off Center Mass	109
Table 7.6: Radiation Efficiency With Off Center Mass	112
Table 7.7: Sound Power And Attenuation With Off Center Mass	118
Table 8.1: Natural Frequencies With Line Mass	125
Table 8.2: Modal Indices With Center Line Mass	128
Table 8.3: Radiation Efficiency With Line Mass	129
Table 8.4: Sound Power And Attenuation With Line Mass	134
Table 9.1: Natural Frequencies With Spring Mass System	142
Table 9.2: Modal Indices With Spring Mass System	144

Table 9.3: Radiation Efficiencies With Spring Mass System 145
Table 9.4: Sound Power and Attenuation With Spring Mass System 149

Chapter 1

Introduction

The Native American Indian lived at peace with the land and as one with nature. Indians were raised to respect and adapt to the environment to sustain their way of life. When people of European heritage came to settle in America, they changed the existing environment to accommodate their needs and desires. The Europeans sought to establish land ownership and boundaries. In order to achieve this goal they used their knowledge, superior weapons and numbers to gain control of the land, and the Native American population.

Although this behavior is characterized throughout history and various cultures, this is merely one example in American history where people strove to control their environment, first by making things bigger, stronger, faster, and easier. They already had guns instead of bows and arrows, and had trains when they did not wish to ride horses. We were learning how to manipulate the world around us to make life easier and more comfortable. Next came running water and then electricity, which lead to many of the modern conveniences we know today such as television, air conditioning, microwaves, computers, lasers, air planes, etc. In addition to creating new devices to help us achieve our goals, whether they be

watching a movie or launching a space shuttle, we are not only developing new devices but also new ideas and technologies to improve many of the modern day conveniences we already have. For example we are trying to design a television with a better picture, a car tire with better traction, a quieter plane ride, or a clearer sounding speaker. These are some of the ways in which man has learned to control his environment.

Control in this context is better described by the word manipulate. In today's technical terms controllability is defined as the ability to transfer a system from any initial state $x(t) = x_i$ to any other state $x_T = x(T)$ in a finite time $T - t \geq 0$, by means of an input [1]. Modern control theory was introduced at the launching of the first sputnik in 1957 by Soviet technology [1]. Today modern control theory is used to control a wide variety of systems. Not only is it implemented in highly technological missile guidance systems, and laser tracking systems, but also more practical systems that ordinary people use everyday such as remote control devices, or even the cruise control on an automobile. In recent times, society has grown to expect an increasing emphasis to be placed on noise control.

1.1 Noise Control

Noise, in this case, refers to unwanted sound which is perceived as an audible

pressure fluctuation in the air or other media [2]. The need for noise control has existed since man began making loud machines such as engines. As he continued to make them bigger, more powerful and more efficient, he inherently made them louder. Noise is especially prominent near highways, and airports, and inside factories, warehouses, planes and cars. This noise is not only an annoyance, but also a safety hazard impeding communication, instilling permanent loss or reduction in hearing ability, and inducing psychological fatigue. This sound can be either air-borne or structure-borne. Structure-borne noise implies sound radiating from a vibrating elastic structure. Studying these systems with the intent of controlling them involves the field of structural acoustics [3]. Structural acoustics is the study of the generation, transmission, and reception of vibrational wave energy coupled between the elastic structure and its media [4]. Structural acoustic control is the process of attenuating this undesirable noise level to an acceptable amount by controlling the dynamics of the structure. This process involves the reduction of energy that the structural noise source converts to sound power and the disruption of the sound transmission paths [2].

Acoustic control has been implemented for years. It started as passive techniques for eliminating noise, such as ear plugs, head phones, and sound absorption board. Passive structural acoustic control involves redesign of the system to change its physical and/or dynamic properties through the use of added mass,

stiffness, damping, and vibration isolators. In application, passive techniques have many limitations. Passive techniques' limitations are primarily dominated by the extreme wavelength of the low frequency sound waves. They do perform well for attenuation of high frequency noise; however, they are not versatile in the fact that they tend to be very case specific in their design and not adaptable to changes. Another type of structural acoustic control that makes up for some of the shortcomings of passive techniques is active control.

The basic principles behind active noise control or cancellation have been understood for quite some time. The idea began as eliminating sound by introducing a copy of the sound (desired to be canceled) which is 180 degrees out of phase, but equal in amplitude. The first formulation of this ideas was introduced in 1933, and a patent was awarded to Lueg in Germany in 1936 [5]. Active noise cancellation is based on destructive interference between the sound fields caused by the "primary" sound source and the introduction of a number of control or "secondary" sound sources [6]. Active noise control works well at reducing low frequency sound radiation, without some of the downfalls of passive techniques such as added size and weight.

Two main techniques of active noise control (ANC) exist, the first of which entails that the "secondary" sources are acoustic sources located around the "primary"

source or structure. This approach is often limited due to space constraints. Another disadvantage of this approach is the possible creation of "control spillover," defined as an increase of noise after control. This control spillover can often be eliminated by optimizing the control source locations [3]. A second type of active acoustic control is Active Structural Acoustic Control (ASAC).

1.2 Active Structural Acoustic Control

ASAC implies that the "secondary" inputs are applied directly to a structure to manipulate the vibration in such a way as to reduce the radiated sound pressure or structure-borne sound. The reality of ASAC has been made possible by technological advances in high speed data acquisition and processing to enable active control implementation in "real time." The introduction of and recent patent on interaction of controller-structure-acoustics by Chris R. Fuller came about at approximately the same time as the concept of "smart structures [7]." The work involved optimizing and reducing the dimensionality of the controller by taking advantage of the natural acoustic coupling of the structure [8]. A smart structure has sensors and actuators attached to its surface or embedded within, and an adaptive control algorithm that is capable of compensation for changes in disturbance inputs [9].

Smart structures were made possible by technological advances in piezoelectric materials, polyvinylidene fluoride (PVDF), and shape memory alloys (SMA). Due to their thermal time constant, the shape memory alloys such as Nitinol 55, are best implemented as actuators for static or low frequency applications. Piezoelectric materials are the dominant actuators used for dynamic active control due to the bandwidth of application. The ceramic most often used as a control actuator in ASAC is lead zirconium titanate (PZT), which was discovered in 1954 by Jaffe [10]. These materials can also be used as sensors; however, it is rarely practical since Kawai discovered the piezoelectric effect in polarized films in 1969 [11]. PVDF has a piezoelectric constant (d_{31}) which is approximately 3 times greater than other tested polarized films. PVDF is four times less dense and 30 times more compliant than PZT, making it the sensor of choice, having a small effect on the dynamics of most structures [9].

Much research work has already been done in the field of ASAC. Fuller and Jones did an experimental investigation on a closed cylindrical elastic shell that was excited by an acoustic source [12]. Point forces applied to the shell exterior were used to control interior sound. The experiment demonstrated the importance of the location and number of sensors and actuators. The best results were obtained when using an equal number of actuators as modes to be controlled. These actuators were also found to work best when located near anti-nodes of the modes

to be controlled. It was also found that using more than one sensor helped eliminate trying to locate a single optimal sensor location where there is a strong response due to all or the modes desired to be controlled.

Fuller makes use of his new technique of reducing noise radiating from a vibrating structure by means of active forces applied directly to the structure, ASAC [13]. In this analytical study a baffled circular plate model was excited by an acoustic plane wave. Quadratic optimization was used to find the optimal control gains to reduce the cost function which was proportional to the radiated acoustic power. It was found that suppressing the plate vibration at selected points did not cause a reduction in the global sound radiation. Significant sound attenuation was achieved by changing the source characteristics of the plate. The lower order response distribution was changed to higher order distribution with a lower radiation efficiency. This was termed "modal restructuring". This work was then experimentally verified and the results confirmed that using microphones as error sensors was a much more efficient means of reducing sound radiation than using accelerometers, due to the fact that the microphones automatically take into account the structural-acoustic coupling [14].

The control force inputs used were applied by the use of electromagnetic shakers which prove to be heavy, cumbersome, and generally require a suitable structure

for their mounting or suspension. These characteristics make them impractical active control inputs, especially when working with lightweight structures. Dimitriadis et al. derived the equations for two-dimensional structures driven by a PZT actuator [14]. In an analytical study of radiation control in a sound transmission investigation, Wang did a comparison between PZT control inputs and electromagnetic shaker inputs [15]. From his work it could be seen that the electromagnetic shaker performed better than the PZT. However taking into account the practicality of implementation, the difference in performance was usually negligible.

Clark performed some experiments on a simply supported flat plate using a harmonic point force excitation and multiple PZT actuators as control forces [16]. It was found that for on resonance excitation, increasing the number of actuators made little improvement in sound attenuation. As expected, the opposite was found for off resonance cases. This is not surprising due to the fact that in an on resonance excitation the acoustic response is dominated by a single structural mode. In the off resonance excitation the response is dictated by a complex interaction of structural modes, thus increasing the number of control actuators allowed more modes to be controlled.

In a further study Clark did work on optimizing sensor and actuator locations to

experimentally verify analytical work done by Wang and Fuller [17,18]. The results matched well for a single and double optimally located actuator, however theory predicted more attenuation with three actuators than was achieved experimentally. This difference was postulated to be nonlinear structural response in addition to the analytical assumption of an "ideal" infinite baffle, not experimentally achievable.

Song developed an optimization procedure for PZT actuator locations and used it to perform an analytical sensitivity study minimizing the far field radiated sound power [19]. His results show that a control system with multiple optimally located actuators demonstrated a good control effect at frequencies other than the design frequency. However, the control effect of these systems was very sensitive to changes in the disturbance location.

Wagstaff proposes a numerical method of selecting control input positions to achieve radiated noise reduction using the boundary finite element software "RAYON", developed by STRACO [20]. The numerical model was used to locate the point force actuators for experimental work using the filtered X-LMS Algorithm. Good agreement was obtained between the theoretical and experimental results for both required control forces and noise reduction to achieve optimum control of a vibrating free plate. This approach can be applied to complex structures.

1.3 Scope and Objective

The primary objective of this work is to study optimization of control actuator forces and locations for complex structures. Complex structures are those which include some kind of discontinuity such as point masses, line masses, and spring mass systems. These systems are difficult to model analytically, not only in theory but also in terms of computational efficiency. The procedure developed here involves modeling the system by means of a finite element model which solves for the nodal displacements of the natural mode shapes due to steady state harmonic excitation. These displacements are then interfaced with the boundary element software package SYSNOISE, which predicts the acoustic pressure at various strategically located field points. This information is then input into a FORTRAN control optimization code which forms a cost function, total radiated sound power, representing the quantity to be minimized. The code then performs a gradient search of the cost function for optimal control actuator locations and their corresponding control forces to reduce the total sound power radiated to the far field. The significance of this approach is that the FORTRAN control optimization code does not need to directly model the various discontinuities. It simply needs the natural frequencies and mode shapes from the finite element solution which directly models the discontinuity, and the corresponding pressure at field points due to these mode shapes from the boundary element solution. The control

approach performs a gradient search of the cost function for the optimal control actuator location and implements Linear Quadratic Optimal Control Theory (LQOCT), discussed later in section 5.2, to solve for the control actuator forces.

1.4 Organization

First an analytical model of a simply supported flat plate will be introduced in Chapter 2. Chapter 2 will discuss the plate solution for the natural frequencies and the models for the point force excitation and the piezoelectric control actuator contribution. The structural response and acoustic response will then be formulated in addition to the objective function to be minimized. Chapter 3 will discuss the assumed modes method for a simply supported flat plate. This will be used for cases with and without point masses, crucial for verification purposes by comparison with the previous model development.

A numerical model will then be developed for the plate response, point force and control actuator contributions. A finite element field point mesh is also developed for formation of the cost function. A boundary element model is then interfaced with the finite element solution and the cost function is formed. A comparison will then be made between the results of this model and the previous two to verify its accuracy.

The control approach is formulated next. Linear Quadratic Optimal Control is discussed for solving for control actuator forces, in addition to the nonlinear optimization of actuator locations. Also discussed are the various design variables, physical constraints, and IMSL codes implemented in the optimization code. Results will be shown from various models of similar systems to verify similar natural frequencies, directivity patterns, and total radiated sound power. Some simple calculations will also be introduced to verify various models. A parametric study will follow, discussing various discontinuities and when these discontinuities become significant with respect to natural frequency, radiation efficiency, directivity patterns, and total radiated sound power. From these results will be drawn some conclusion and an overall evaluation of the procedure will be given, with recommendations for improvement and expansion.

The control approach is formulated next. Linear Quadratic Optimal Control is discussed for solving for control actuator forces, in addition to the nonlinear optimization of actuator locations. Also discussed are the various design variables, physical constraints, and IMSL codes implemented in the optimization code. Results will be shown from various models of similar systems to verify similar natural frequencies, directivity patterns, and total radiated sound power. Some simple calculations will also be introduced to verify various models. A parametric study will follow, discussing various discontinuities and when these discontinuities become significant with respect to natural frequency, radiation efficiency, directivity patterns, and total radiated sound power. From these results will be drawn some conclusion and an overall evaluation of the procedure will be given, with recommendations for improvement and expansion.

Chapter 2

Analytical Model

In order to develop an accurate model of a complex structure it is important to first develop a model of a simple structure with a known closed form solution to which the complex model can be simplified and compared. This section will develop the formulation for a simply supported flat plate excited by a single frequency disturbance, commonly referred to as the primary source. Chapter 3 will develop a theoretical model using the assumed modes method, followed by a Chapter 4 which will develop a numerical model. The results from these three models will then be compared for the simply supported flat plate solutions without discontinuities. Subsequently, the assumed modes model will be compared with the numerical model for a complex structure, a simply supported flat plate with a point mass on it.

2.1 Dynamic Response

The simply supported flat plate is made of steel with dimensions .38 X .30 X 1.96E-3 meters. The material properties are itemized in Table 2.1, and the coordinate system is shown in Figure 2.1. The displacement response for a simply

supported flat plate in terms of its modal decomposition is as follows [21]:

$$w(x,y,t) = \sum_{m=1}^{\infty} \sum_{n=1}^{\infty} W_{mn} \sin(\gamma_m x) \sin(\gamma_n y) \exp(j\omega t) \quad (2.1)$$

where:

m and n = Modal indices

$$\gamma_m = m\pi/L_x$$

$$\gamma_n = n\pi/L_y$$

W_{mn} = modal amplitudes

L_x = plate length in x direction

L_y = plate length in y direction

ω = driving frequency

t = time

Table 2.1: Steel Plate Material Properties

Property	Symbol	Value	Units
Elastic Modulus	E	20.4E+10	N/m ²
Density	ρ	7700	kg/m ³
Poisson's Ratio	μ	.28	-
Damping Ratio	ν	.001	-

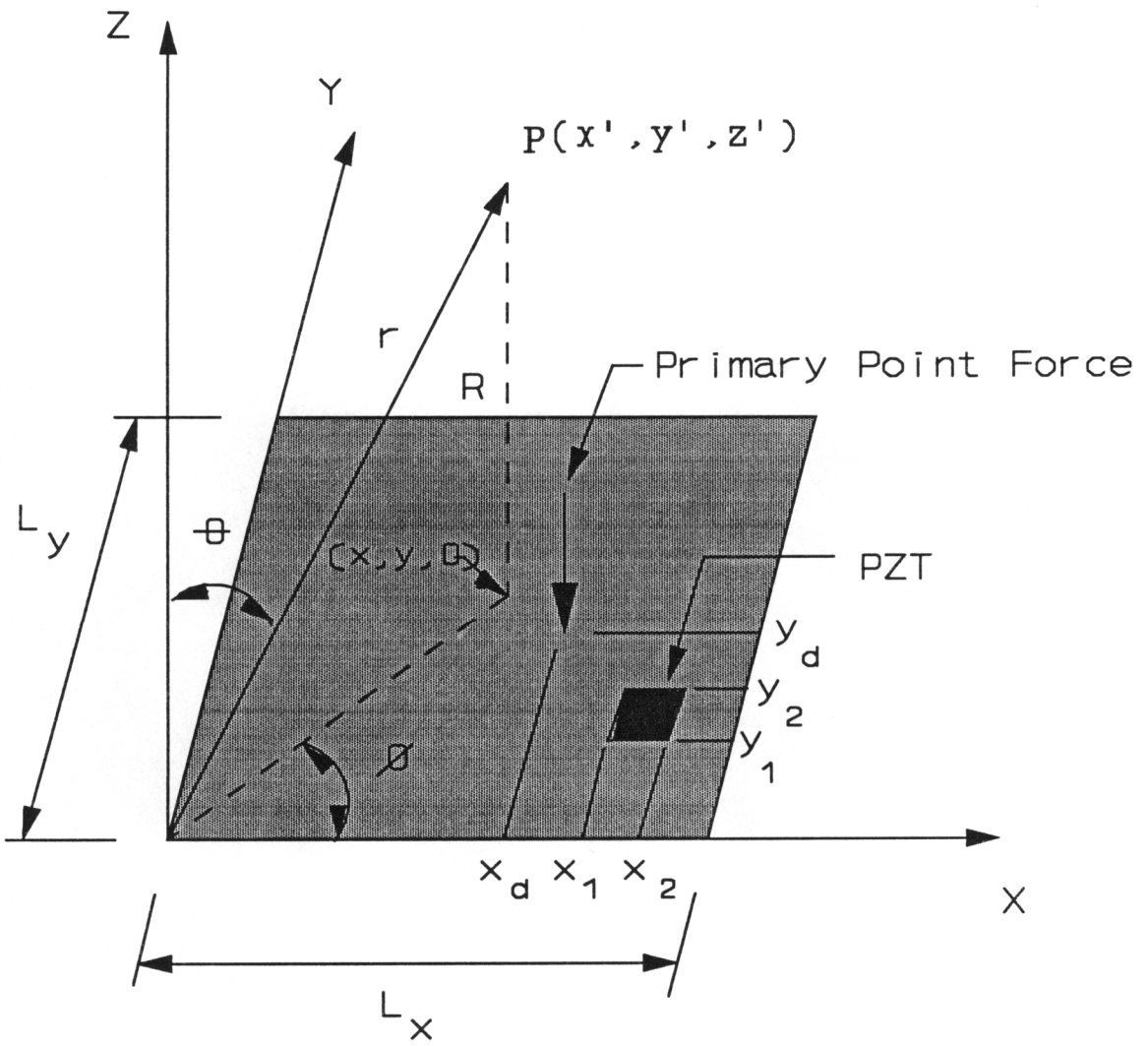


Figure 2.1: Plate Coordinate System

Due to computational constraints, the summations over an infinite number of modes in equation (2.1) above, are limited to finite summations as discussed later in Chapter 6.

2.2 Point Force Model

The modal amplitudes of a simply supported flat plate excited by a harmonic point force, primary force F of unit magnitude, at the disturbance location (x_d, y_d) as shown in Figure 2.1, are obtained by solving its equation of motion as follows [21]:

$$W_{mn}^P = \frac{4F \sin(\gamma_m x_d) \sin(\gamma_n y_d)}{\rho'' L_x L_y (\omega_{mn}^2 - \omega^2 + j2\eta\omega\omega_{mn})} \quad (2.2)$$

The resonant frequencies of the simply supported flat plate used in the above equation can be found from:

$$\omega_{mn}^2 = \frac{D_e}{\rho''} [(\gamma_m)^2 + (\gamma_n)^2]^2 \quad (2.3)$$

where flexural stiffness of the plate is defined by:

$$D_e = \frac{Eh^3}{12(1-\nu^2)} \quad (2.4)$$

and

E = Young's modulus of the plate

h = plate thickness

ν = Poisson's ratio

η = damping ratio

ρ'' = plate mass density per unit area

2.3 Piezoceramic Actuator Model

In order to simulate the control inputs, a model of the piezoelectric actuator effects is needed. The piezoelectric elements modeled in this study are G-1195 lead zirconium titanate, which has properties listed in Table 2.2. The PZT actuator is of fixed size, and is modeled as an actuator pair mounted in the same location on both the top and bottom of the plate surface as shown in Figure 2.2. These actuators would then be wired 180° out of phase to induce a case of pure bending about the neutral axis. Dimitriadis et al. shows that these distributed actuators can be modeled by applying line moments to the plate at the actuator edges [14].

The simply supported flat plate with a mounted piezoelectric actuator pair has a modal response due to secondary forces that can be derived as follows [14]:

Table 2.2: PZT Material Properties

Property	Symbol	Value	Unit
PZT Strain Coefficient	d_{31}	166E-12	m/V
Density	ρ	7600	kg/m ³
Elastic Modulus	E_{33}	4.9E+10	N/m ²
Elastic Modulus	E_{11}	6.3E+10	N/m ²

$$W_{mn}^s = \frac{4C_o \varepsilon_{pe}}{\rho'' L_x L_y (\omega_{mn}^2 - \omega^2 + j2\eta\omega\omega_{mn})} \left(\frac{\gamma_m^2 + \gamma_n^2}{\gamma_m \gamma_n} \right) X[(\cos(\gamma_m x_1^s) - \cos(\gamma_m x_2^s))(\cos(\gamma_n y_1^s) - \cos(\gamma_n y_2^s))] \quad (2.5)$$

The constants used in the above equation are defined as follows:

$$\varepsilon_{pe} = \frac{d_{31} V^s}{t} \quad (2.6)$$

$$C_o = -\frac{Eh(1+\nu)}{6(1-\nu)} \frac{P}{(1+\nu - (1+\nu_{pe})P)} \quad (2.7)$$

$$P = -\frac{E_{pe}(1-\nu^2)}{E(1-\nu_{pe}^2)} K \quad (2.8)$$

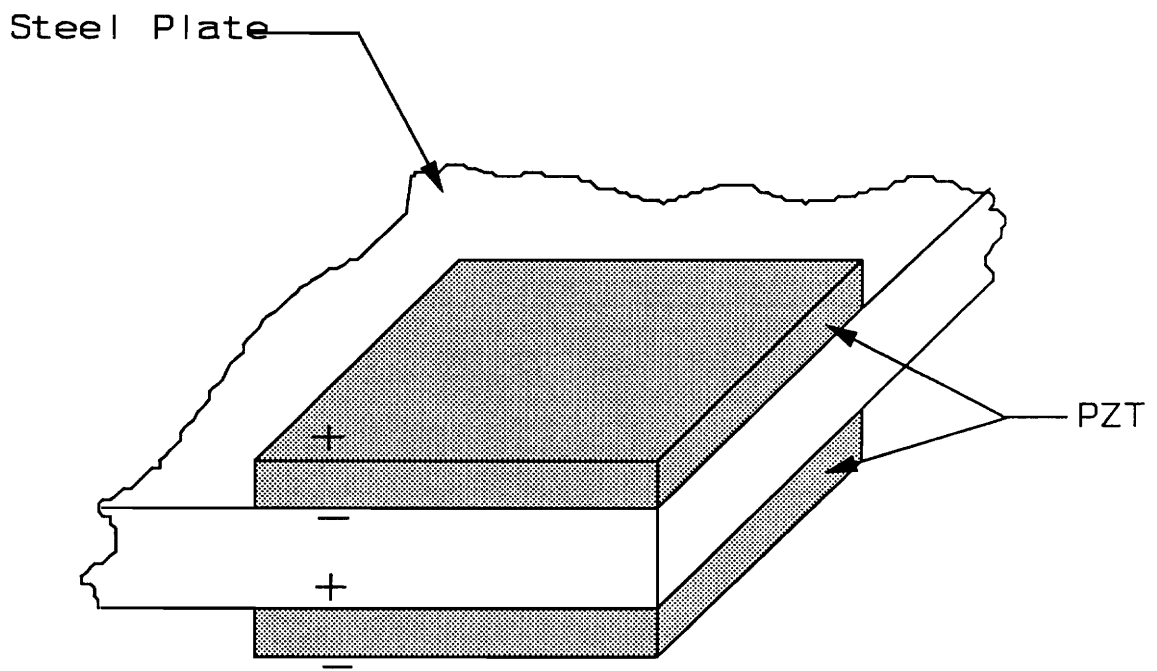


Figure 2.2: Schematic of PZT Actuator Pair

$$K = \frac{6th(h+t)}{(h^3 + 8t^3) + 6ht^2} \quad (2.9)$$

where:

(x_1^s, y_1^s) = coordinates of lower left corner of S^{th} actuator

(x_2^s, y_2^s) = coordinates of upper right corner of S^{th} actuator

V^s = complex voltage of S^{th} actuator

t = thickness of piezo patch

E_{pe} = Young's modulus of piezo patch

ν_{pe} = Poisson's ratio of piezo patch

2.4 Total Structural Response

The total structural response of the simply supported flat plate can be obtained by the summation of modal amplitudes due to the point force disturbance input and due to each of the PZT actuator pairs. The total modal response to be used in equation (2.1) is obtained as follows:

$$W_{mn} = W_{mn}^P + \sum_{s=1}^S W_{mn}^S \quad (2.10)$$

where S is the number of secondary sources, or control actuator pairs.

2.5 Acoustic Response

The simply supported flat plate has an analytical expression for the structural and acoustic response. Rayleigh's integral can be evaluated at acoustic field points to give an approximation of the far field pressure. To be considered a point in the acoustic far field the following requirements must be satisfied [22]:

$$R \gg \lambda, R \gg l, R \gg \frac{\pi l^2}{2\lambda} \quad (2.11)$$

where R is the distance from the source to the field point, λ is the wavelength of the radiated sound, and l is the maximum source dimension.

The formulation for Rayleigh's integral is as follows:

$$p(r,t) = \frac{j\omega\rho_0}{2\pi} \int_S \frac{v_n(r_s) \exp(-j\omega R)}{R} dS \quad (2.12)$$

where:

ρ_0 = density of the media

r = the position vector of the acoustic field point

r_s = the position vector along the elemental surface

S = the elemental surface

$v_n(r_s) =$ the normal velocity

$R =$ the magnitude of the vector $r - r_s$

The coordinate system used to compute the acoustic pressure for the plate is shown in Figure 2.1. Differentiating equation (2.1) with respect to time gives an expression for the velocity of the simply supported plate. Substituting this expression into Rayleigh's integral yields an expression for the radiated sound at a chosen field point as follows:

$$p(x', y', z', t) = -\frac{\omega^2 \rho_0}{2\pi} \exp(j\omega t) \sum_{n=1}^N \sum_{m=1}^M W_{mn} \int_0^{L_x} \int_0^{L_y} \sin\left(\frac{m\pi x}{L_x}\right) \sin\left(\frac{n\pi y}{L_y}\right) \times \exp(jk \frac{\sqrt{(x'-x)^2 + (y'-y)^2 + (z')^2}}{\sqrt{(x'-x)^2 + (y'-y)^2 + (z')^2}}) dy dx \quad (2.13)$$

where:

(x', y', z') = spatial coordinates of the acoustic field

(x, y, z) = spatial coordinates on the plate

The coordinate system used in the above expression is also that shown in Figure 2.1 and corresponds to that used by Wallace which contains this analysis in greater detail [23].

2.6 Objective Function

The objective of this research is to develop a procedure to optimize the control forces and locations on complex structures in order to reduce far field sound radiation from the structure. Global reduction of far field radiated sound is desired, therefore the logical choice for the objective function, or cost function to be minimized is the total radiated far field sound power. Total radiated sound power is calculated by integrating the square of the radiated sound pressure over a hemisphere about the structure. This objective function is used by Wang et al. and is formulated as follows [24]:

$$\Phi_p = \frac{1}{R^2} \int_0^{2\pi} \int_0^{\frac{\pi}{2}} |p_t|^2 \sin(\theta) d\theta d\phi \quad (2.14)$$

where R is the radius of the hemisphere and p_t is the complex pressure at that particular point on the hemisphere.

This double integration over a hemisphere of the far field sound pressures found by the Rayleigh integral is a very computational intensive calculation. Wang et al. used a finite sum of the mean square radiated sound pressure measured at appropriately located microphones as an estimate of this objective function [23]. By this method the objective function integral is discretized into the following summation:

$$\Psi = \sum_{i=1}^I |p_t(R_i, \theta_i, \phi_i)|^2 \quad (2.15)$$

where I is the number of microphones. There is a trade off in choosing the number of microphones; i.e., there must be enough to achieve an accurate estimate of the objective function without reverting back to the original problem of extensive computational time.

The microphone locations for this model are those used by Clark. Clark uses nine discrete field points over a hemisphere of radius 1.8 meters, to estimate the objective function [9]. These nine points whose coordinates can be seen in Table 2.3 are shown in Figure 2.3. The coordinate system of this objective function was then translated into the coordinate system used in the plate model shown in Figure 2.1. The pressure at each of these field points to be used in the objective function equation (2.14), is evaluated using Wallace's expression for far field acoustic radiation from a baffled simply supported plate as follows [23]:

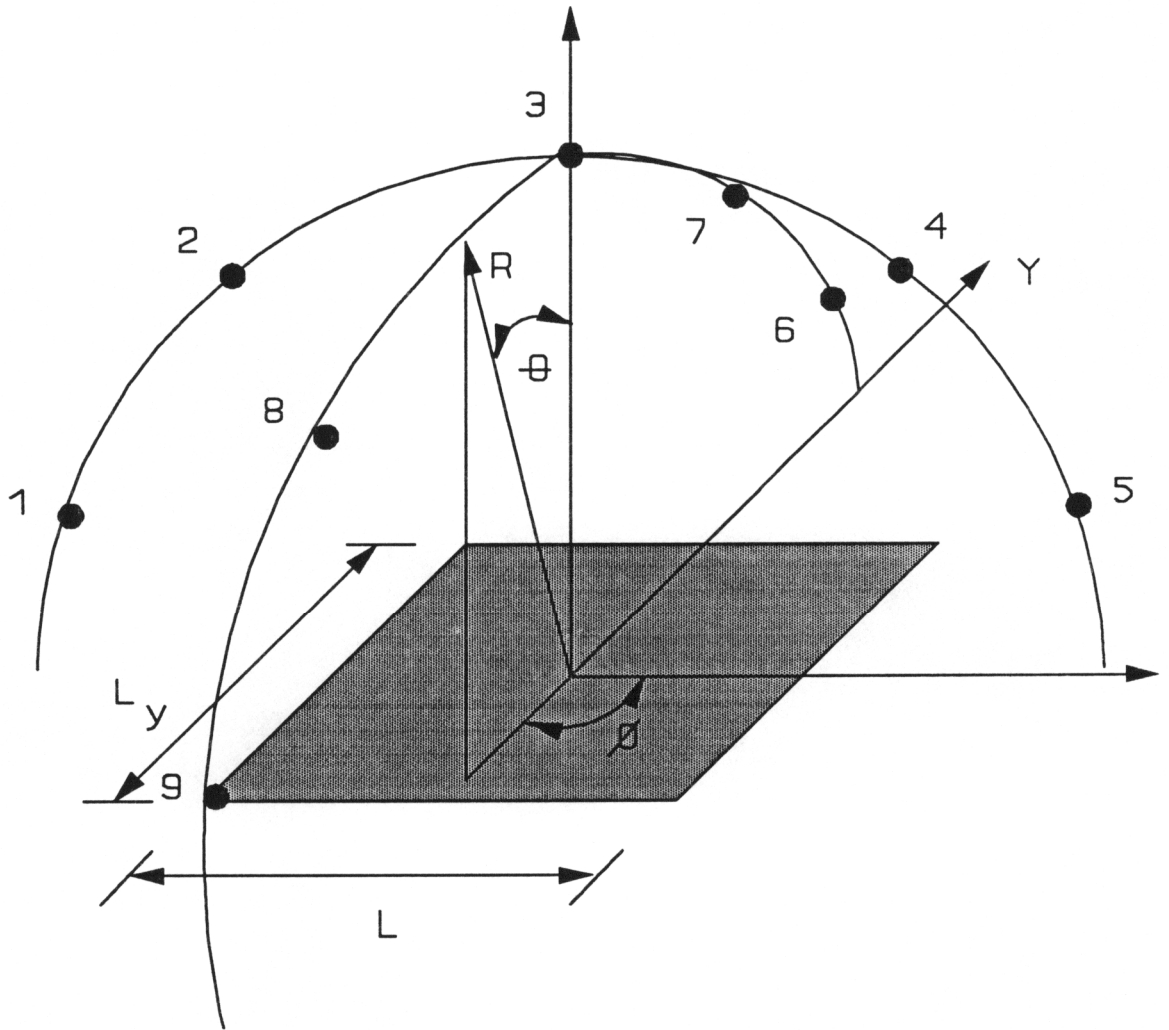


Figure 2.3: Objective Function Coordinate System

Table 2.3: Objective Function Coordinates

Location	θ	ϕ
1	75	180
2	45	180
3	0	0
4	45	0
5	75	0
6	75	90
7	45	90
8	45	270
9	75	270

$$p(r, \theta, \phi, t) = \frac{k\rho_0 c L_x L_y \exp(-jkr)}{2\pi^3 r} \sum_{m=1}^{\infty} \sum_{n=1}^{\infty} \frac{W_{mn}}{mn} \left[\frac{(-1)^m \exp(-j\alpha) - 1}{(\alpha/m\pi)^2 - 1} \right] \times \left[\frac{(-1)^n \exp(-j\beta) - 1}{(\beta/n\pi)^2 - 1} \right] \exp(j\omega t) \quad (2.16)$$

where

$$\alpha = kL_x \sin(\theta) \cos(\phi) \quad (2.17)$$

$$\beta = kL_y \sin(\theta) \sin(\phi) \quad (2.18)$$

and

r = radius to the field point

k = acoustic wave number in media (ω/c)

c = speed of sound in media

ρ_o = density of media

Chapter 3

Assumed Modes Method

This section will develop a model for the complex system of a simply supported flat plate with a point mass on it using the assumed modes method. In Chapter 6 this model will later be evaluated with a point mass of zero to be compared with the analytical model developed in the Chapter 2. The model will then be evaluated with a point mass and used to verify the accuracy of the numerical model that will be developed in Chapter 4.

3.1 Eigenvalue Formulation

This model will be very similar to the model in the previous section, Chapter 2, and will use much of the same development. The main difference is that the assumed modes method will be used to build a mass matrix so that the eigenvalue problem may be solved for the new natural frequencies of the plate with a point mass on the surface. It is then possible to solve for the eigenfunction matrix which will be used to weight the equations for various responses. The modal indices will be indexed using a single parameter with values corresponding to those in an example set tabulated in Table 3.1. These indices have been previously sorted by

ordering the natural frequencies for the new system from lowest to highest. These new natural frequencies are found later in the solution to equation (3.6) , and vary, along with their corresponding modal indices, with variations in the magnitude and location of the point mass.

Table 3.1: Modal Indices

i	m	n
1	1	1
2	2	1
3	1	2
4	2	2
5	3	1
6	3	2
7	1	3
8	4	1
9	2	3
10	4	2
11	3	3

The mass normalized mode shapes for the uniform plate can be computed by the following equation [21]:

$$\phi_i(x,y) = \frac{2}{\sqrt{\rho'' L_x L_y}} \sin\left(\frac{m_i \pi x}{L_x}\right) \sin\left(\frac{n_i \pi y}{L_y}\right) \quad (3.1)$$

If a point mass (m_p) exists, the above equation is evaluated at the coordinates of that point mass (x_m, y_m) giving the modal forces, $\phi_i(x_m, y_m) = \Psi_i$. The mass matrix can now be constructed from a combination of these mode shapes in the following manner:

$$[M] = [I] + \begin{bmatrix} \Psi_1^2 & \Psi_1 \Psi_2 & \Psi_1 \Psi_3 \dots \\ \Psi_1 \Psi_2 & \Psi_2^2 & \Psi_3 \Psi_2 \dots \\ \dots & \dots & \dots \dots \end{bmatrix} m_p \quad (3.2)$$

The stiffness matrix is then constructed from the natural frequencies of the uniform plate without the point mass, as computed in equation (2.3). The equation for calculating the frequencies now has a single index corresponding to Table 3.1 as follows:

$$\omega_i^2 = \frac{De}{\rho''} [(\gamma_m)^2 + (\gamma_n)^2]^2 \quad (3.3)$$

where:

$$\gamma_m = \frac{m_i \pi}{L_x} \quad \gamma_n = \frac{n_i \pi}{L_y} \quad (3.4)$$

These natural frequencies lie along the diagonal of the matrix and the off diagonal terms are zeros:

$$[K] = \begin{bmatrix} \omega_1^2 & 0 & 0 & \dots \\ 0 & \omega_2^2 & 0 & \dots \\ \dots & \dots & \dots & \dots \end{bmatrix} \quad (3.5)$$

The classic eigenvalue problem is then formed:

$$[K] - (\omega_i^2)[M] = [0] \quad (3.6)$$

Solving this classic eigenvalue problem yields the new natural frequencies (ω_n) of the system and their corresponding eigenvectors. These eigenvectors are put in the form of an i by i matrix $[E]_{ki}$ and used to modify the previous analytical model of Chapter 2, such that it can calculate the response of the complex model of a simply supported flat plate with a point mass on it.

3.2 Point Force Model

In order to obtain the modal response to a harmonic point force disturbance, for a simply supported flat plate with a point mass discontinuity, equation (2.2) must be modified to incorporate the eigenfunction matrix found via the eigenvalue

problem solution in the previous section. Equation (2.2) for finding the modal response for the simple structure due to the primary force must be multiplied by this eigenfunction matrix $[E]_{ki}$ to form the modal response for the simply supported flat plate with a point mass discontinuity, due to the primary force as follows:

$$W_i^P = \frac{4F}{\rho'' L_x L_y} \frac{\sum_{k=1}^K [E]_{ki} \sin(\gamma_{m_k} x_d) \sin(\gamma_{n_k} y_d)}{(\omega_{n_k}^2 - \omega^2 + j2\eta\omega\omega_{n_k})} \quad (3.7)$$

3.3 Piezoceramic Actuator Model

The modal amplitudes for a piezoceramic actuator pair can likewise be modeled by incorporating the eigenvalue matrix into the simpler model in equation (2.5). Equation (2.5) for the modal response of the simple structure due to the secondary forces must also be multiplied by the eigenvalue matrix $[E]_{ki}$ to form the modal response of the simply supported flat plate with a point mass discontinuity on it, due to the secondary forces as follows:

$$W_i^S = \frac{4C_o \epsilon_{pe}}{\rho'' L_x L_y} \frac{\sum_{k=1}^K [E]_{ki} \left(-\frac{\gamma_{m_k}^2 + \gamma_{n_k}^2}{\gamma_{m_k} \gamma_{n_k}} \right)}{(\omega_{n_k}^2 - \omega^2 + j2\eta\omega\omega_{n_k})} X[(\cos(\gamma_{m_k} x_1^S) - \cos(\gamma_{n_k} x_2^S))(\cos(\gamma_{m_k} y_1^S) - \cos(\gamma_{n_k} y_2^S))] \quad (3.8)$$

whose constants are the same as those defined in equations (2.6) through (2.9).

3.4 Total Structural Response

The modal amplitudes used to calculate the total structural response of a simply supported flat plate containing a discontinuity, and excited by a harmonic point force can be calculated just as was done in equation (2.10) except this formulation will continue to use a single index as follows:

$$W_i = W_i^P + \sum_{s=1}^S W_i^S \quad (3.9)$$

This summation of the primary and secondary modal amplitudes can then be substituted into the single index version of equation (2.1) as shown:

$$w(x,y,t) = \sum_{i=1}^{\infty} W_i \sin(\gamma_m x) \sin(\gamma_n y) \exp(j\omega t) \quad (3.10)$$

3.5 Acoustic Response

Using the same formulation as in the previous model, the sound pressure at the predetermined field points listed in Table 2.3 can be calculated by converting Wallace's expression in equation (2.16) to correspond with the single modal index

model as follows [23]:

$$p(r, \theta, \phi, t) = \frac{k\rho_0 c L_x L_y}{2\pi^3 r} \sum_{i=1}^N \frac{W_i}{m_i n_i} \left[\frac{(-1)^m \exp(-j\alpha) - 1}{(\alpha/m_i \pi)^2 - 1} \right] \times \left[\frac{(-1)^n \exp(-j\beta) - 1}{(\beta/n_i \pi)^2 - 1} \right] \exp(j\omega t) \quad (3.11)$$

3.6 Objective Function

The objective function is also formed the same as it was in the previous model using equation (2.15) as a summation approximation to the double integral of the sound pressure over a hemisphere. The field points for the summation over the hemisphere are the same as those listed in Table 2.3 used in the previous model. These field points are also shown in Figure 2.3.

Chapter 4

Numerical Model

The previous two chapters develop analytical models for a simply supported plate with and without a point mass. This chapter will develop a numerical model that will be evaluated for consistency with the previously developed models. The numerical model will then be used to study actuator optimization for complex structures with various discontinuities.

4.1 Finite Element Model

This numerical model consists partly of a finite element model developed here, for which the preliminary work was done in finite element software package IDEAS level 4.1. IDEAS stands for Integrated Design Engineering Analysis Software and is a product of Structural Dynamics Research Corporation (SDRC). Later results came from the updated finite element software package CAEDS version 4.2 for IBM host workstations, also a product of SDRC. The first step in developing this finite element model is to generate a mesh representing the plate. This mesh will be composed of nodes and elements. Some primary considerations must be made as to the size of the mesh. In general, the finer the mesh is (i.e. more elements

of smaller size) the more accurate the model will be. However, there is a tradeoff here between numerical accuracy and computational time. The rule of thumb is that an accurate model should have four to six nodes per wavelength of the highest mode shape frequency [25]. In this study we are typically including the first eleven natural mode shapes. Assuming these first eleven modes have similar indices as the example case tabulated in Table 3.1, the highest single index is four. This would imply that a conservative computational approach would yield no fewer than sixteen nodes in each direction. Another important aspect of a good mesh is that the elements should be square or as close to square as possible. In light of these considerations, along with given physical dimensions, it was decided to create a mesh that had 360 nodes and 323 elements, being nineteen elements wide and seventeen elements tall. These shell elements are close to being square in that the length in the Y direction is eighty-eight percent of the length in the X direction. The corresponding physical and material property tables are then created or modified from default to correspond with the previous models, see Table 2.1. Originally the mesh was much courser and was refined until the difference in the plate solution was within a fraction of a percent, also corresponding with the above element size decision.

In order to model the simply supported end conditions the nodes along the edge of the plate must be restrained. These nodes have six degrees of freedom (d.o.f.):

translation in the X, Y, and Z direction, and rotation about the X, Y, and Z axis. In order to model the simply supported boundary conditions, all nodes along the plate edge must be restricted from translation in all three directions. In addition, the nodes along the edge of the plate parallel to one axis should be allowed to rotate about that axis, but should be restrained from rotation about the other two axes. This implies that the nodes at the corner will be restrained from rotation about all three axes. Due to practical physical restraints, the in plane rotation of all nodes will also be restrained, i.e. rotation about the Z axis.

For this study the plate model is developed from thin shell elements. Each element is represented by a stiffness matrix, a mass matrix, and potentially a damping matrix. The objective of the finite element model is ultimately to find nodal displacements. The relationship between the nodal displacements and nodal forces is described by the element stiffness matrices. There are various methods for formulating these stiffness matrices such as; directly using physical reasoning, variational or energy methods, and weighted residual methods [26]. For this work the energy method is used to calculate the stiffness matrices. Various methods also exist for formation of element mass matrices. The two main methods are the "consistent" and the "lumped-mass" matrix formulation [27]. The consistent formulation uses the same finite element displacement field to construct mass matrices as that used to construct the stiffness matrices. The result is a banded

mass matrix with a fill pattern similar to the stiffness matrix. The lumped-mass formulation is a method for constructing a diagonal mass matrix from the consistent mass matrix. The lumped mass matrix formulation lumps point masses at element nodes. The distribution of mass at each particular node is found by various methods. Some methods divide the mass up evenly while others use scaled diagonal terms of the consistent mass matrix to preserve the total element mass. Because lumped-mass matrices typically have only diagonal terms they have computational advantages during calculations and storage.

It can be shown that the natural frequency associated with a mode shape of a finite element model is always greater than or equal to the corresponding exact natural frequency of the undiscretized mathematical statement of the structural vibration problem. Mass lumping is a technique used to soften the discretized model, which can improve the accuracy of the natural frequencies, but the upper bound nature of the frequencies is lost [27]. For refined meshes the lumped-mass matrix formulation works well and reduces the difficulties with two off-diagonal terms, whereas the consistent method performs better with course meshes due to the influence of rotary inertia terms at the nodes [28]. For this model the mass lumping matrix formulation was used and mesh refinement was implemented until frequency convergence was achieved.

Upon connecting the elements the mass and stiffness matrices for the full structure are created. The element stiffness matrix coefficients are summed to form the structure stiffness matrix, [K]. The structure mass matrix, [M], is similarly formed from the element mass matrices. Having formed the mass and stiffness matrix for the structure, the eigenvalue problem can be formed as follows:

$$([K] - \lambda[M])\{A\} = \{0\} \quad (4.1)$$

The above equation (4.1) is valid when using the following assumptions:

- Free vibration, no external loads applied
- No damping, coefficients of damping matrix [C] are zeroed
- Harmonic motion, each d.o.f. has sinusoidal motion of the same frequency.

The eigenvalue problem, equation (4.1), is then solved for the eigenvalues, $\lambda_r = \omega_r^2$. For each of these eigenvalues there is a corresponding eigenvector, $\{A\}_r$, which is a set of nodal displacements also obtained from equation (4.1). These eigenvectors can be "mass normalized" such that each modal mass is unity as follows:

$$m_r = \{\phi\}_r^T [M] \{\phi\}_r = 1 \quad (4.2)$$

where $\{\phi\}_r$ is the mass normalized mode shape corresponding to ω_r , and m_r is the r^{th} coefficient in the modal mass matrix. If the same operation is performed on the modal stiffness the following results:

$$k_r = \{\phi\}_r^T [K] \{\phi\}_r = \omega_r^2 \quad (4.3)$$

These eigenvectors also possess the unique property of orthogonality with respect to the symmetric mass and stiffness matrices:

$$\{\phi\}_j^T [M] \{\phi\}_k = \{\phi\}_j^T [K] \{\phi\}_k = 0 \quad (j \neq k) \quad (4.4)$$

This orthogonality is what allows the decoupling of the system dynamic equation of motion shown below:

$$[M]\{\ddot{D}\} + [C]\{\dot{D}\} + [K]\{D\} = \{F\} \quad (4.5)$$

where $[C]$ is the structure damping matrix, $\{F\}$ is the external load on the structure, and $\{D\}$ is the structural displacement of the nodes.

4.1.1 Point Force Model

Having developed the "free vibration" solution for a structure, this section will

develop the procedure for obtaining the "forced response" solution for a structure. Solving the finite element model for a forced response takes a great deal of time and effort. This takes into account not only the significant computational effort of solving a forced response, but also the interactive operator time. The operator must first recalculate the free vibration solution with slight variations in the solution control options. The iterative solution for calculating the natural frequencies and mode shapes must be changed from solution no restart to solution restart with initial conditions. Solution no restart implies starting the iterative process toward convergence with no prior knowledge, or matrix development. Solution restart with initial solution allows the iterative process to restart where it left off if convergence criteria is not met. The operator must also opt to keep the hypermatrix containing information to be used in the forced response solution such as the matrices used in the solution restart with initial solution. The free vibration case is then solved again with these new settings.

In the system dynamics module, the model must be expanded to define components which are then combined to create the system. This component definition can be used for things such as complex structures, or iterative modeling in which components are being added. The next step is to complete the excitation definition where the forcing function is defined. The loads on the components must then be calculated and read into the model. The model is then ready to be solved

for the forced response. However, the sophisticated numerical model used in this work employs the procedure developed below which eliminates much of this work and computational effort by means of an analytical method using numerical results previously found from the free vibration solution only, thus making the forced response calculation unnecessary. The results of this method were verified with the forced response finite element solution which is discussed further in Chapter 6.

The dynamic response of a simply supported plate excited by a harmonic point force is governed by the following equation:

$$X(\omega) = \sum_{n=1}^N F f_n \phi_n H_n(\omega) \exp(j\omega t) \quad (4.6)$$

where:

N = the number of modes included in the analysis

F = the primary force or disturbance assumed to be real and of unit magnitude

f_n = the modal force

ϕ_n = the mode shape vector obtained from the finite element model

H_n = the frequency response function

ω = the excitation frequency

The above equation assumes that the mode shapes are normalized with respect

to the mass matrix. This is achieved by dividing the Z direction displacement of the mode shape by the square root of the modal mass for that mode shape. The disturbance is a harmonic point force located at (x_d, y_d) . The associated modal forces are mass normalized mode shapes evaluated at the excitation location:

$$\hat{f}_n = \phi_n(x_d, y_d) \quad (4.7)$$

and the frequency response function is defined as:

$$H_n(\omega) = \frac{1}{\omega_n^2 - \omega^2 + 2j\beta_n\omega_n\omega} \quad (4.8)$$

where:

ω_n = the natural frequency

β_n = the damping ratio (.001)

4.1.2 Piezo Actuator Model

The dynamic response of a simply supported flat plate, excited by the harmonic point force above, with applied piezoelectric control actuation is governed by the following equation:

$$X(\omega) = \sum_{n=1}^N (F\hat{f}_n + \sum_{i=1}^{Na} U_{ni}M_i)\phi_n H_n(\omega) \exp(j\omega t) \quad (4.9)$$

where:

N_a = the number of actuators

U_{ni} = the control modal force

M_i = the control moment assumed to be of unit magnitude

The control modal forces for the above equation are obtained from manipulation of information contained in the mass normalized finite element mode shape files. These mode shapes contain the displacement in the X, Y, and Z direction, and the rotation about the X, Y, and Z axis for each node. The control modal forces are formulated by the following equation which is derived below:

$$U_{ni} = M_o \left[\frac{(R_{x_2, y_1} - R_{x_1, y_1})}{2} (x_2 - x_1) - \frac{(R_{x_2, y_2} - R_{x_1, y_2})}{2} (x_2 - x_1) \right. \\ \left. + \frac{(R_{x_1, y_2} - R_{x_1, y_1})}{2} (y_2 - y_1) - \frac{(R_{x_2, y_2} - R_{x_2, y_1})}{2} (y_2 - y_1) \right] \quad (4.10)$$

where $R_{x,y}$ are the rotations corresponding to the X and Y coordinates of the piezo patch as shown in Figure 4.1A, and $M_o = M_x = M_y$ where M_x and M_y are the complex line moments at the actuator edges. During optimization of the piezo patch location, its coordinates seldom correspond with the finite element nodes for which the rotations are known. To overcome this, the required rotation values are found by using a two dimensional surface fit (cubic spline). The spline used is a modified version of the subroutine called Ibiran, an IMSL routine IQHSCV as modified by Computer Science Corp. at Hampton Virginia, August 15, 1983.

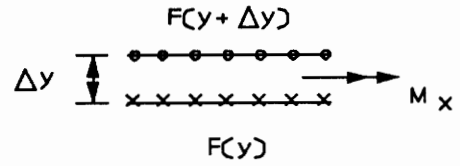
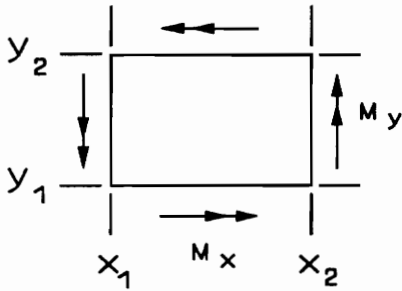


Figure 4.1A: Line Moment Piezo Model,

B: Line Moment

Equation (4.10) above is derived as follows: The control forces are modeled as line moments, as shown in Figure 4.1A. A line moment equation can be derived from a line couple, as shown in Figure 4.1B. M_x can be modeled as two equal and opposite line forces ($F(y+\Delta y)$ coming out of the page, and $f(y)$ going into the page) separated by a finite distance (Δy), as Δy approaches zero, as long as Δ is much less than λ . The line moment contribution to the control modal force is governed by the following equation:

$$U_{mx} = \int_{x_1}^{x_2} \phi_n(x, y_1 + \Delta y) F(y_1 + \Delta y) dx - \int_{x_1}^{x_2} \phi_n(x, y_1) F(y_1) dx \quad (4.11)$$

To be a couple, $F(y+\Delta y)$ must be equal to $F(y)$, and therefore equal to $F(y_1)$. The line moment M_x must remain constant and is governed by:

$$M_x = F\Delta y = \text{const} \quad \therefore \quad F = \frac{M_x}{\Delta y} \quad (4.12)$$

using this substitution and introducing the limit as Δy goes to zero the following equation is obtained:

$$U_{nx} = \int_{x_1}^{x_2} \lim_{\Delta y \rightarrow 0} \frac{\phi_n(x, y_1 + \Delta y) - \phi_n(x, y_1)}{\Delta y} M_x \, dx \quad (4.13)$$

From the fundamental theorem of calculus this equation becomes [29]:

$$U_{nx} = \int_{x_1}^{x_2} \frac{\partial \phi_n(x, y_1)}{\partial y} dx M_x \quad (4.14)$$

Using the above substitution and the assumption that $M_x = M_y = M_o$, the control modal force equation for the piezo, taking all four line moments into account can be written as:

$$U_n = \int_{x_1}^{x_2} \frac{\partial \phi_n(x, y_1)}{\partial y} M_o \, dx - \int_{x_1}^{x_2} \frac{\partial \phi_n(x, y_2)}{\partial y} M_o \, dx + \int_{y_1}^{y_2} \frac{\partial \phi_n(x_1, y)}{\partial x} M_o \, dy - \int_{y_1}^{y_2} \frac{\partial \phi_n(x_2, y)}{\partial x} M_o \, dy \quad (4.15)$$

where:

$$\phi_n(x,y) = \sin\left(\frac{\pi x}{L_x}\right) \sin\left(\frac{\pi y}{L_y}\right) \quad (4.16)$$

therefore for mode one:

$$\begin{aligned} \frac{\partial \phi}{\partial y} &= \frac{\pi}{L_y} \sin\left(\frac{\pi x}{L_x}\right) \cos\left(\frac{\pi y}{L_y}\right) \\ \frac{\partial \phi}{\partial x} &= \frac{\pi}{L_x} \cos\left(\frac{\pi x}{L_x}\right) \sin\left(\frac{\pi y}{L_y}\right) \end{aligned} \quad (4.17)$$

using the above substitutions and integrating, the control modal force equation for the piezo is obtained:

$$\begin{aligned} U_n &= \left(-\frac{L_x}{L_y} M_o \cos\left(\frac{\pi x}{L_x}\right) \cos\left(\frac{\pi y_1}{L_y}\right)\right) \Big|_{x_1}^{x_2} + \left(\frac{L_x}{L_y} M_o \cos\left(\frac{\pi x}{L_x}\right) \cos\left(\frac{\pi y_1}{L_y}\right)\right) \Big|_{x_1}^{x_2} \\ &+ \left(-\frac{L_y}{L_x} M_o \cos\left(\frac{\pi x_1}{L_x}\right) \cos\left(\frac{\pi y}{L_y}\right)\right) \Big|_{y_1}^{y_2} + \left(\frac{L_y}{L_x} M_o \cos\left(\frac{\pi x_2}{L_x}\right) \cos\left(\frac{\pi y}{L_y}\right)\right) \Big|_{y_1}^{y_2} \end{aligned} \quad (4.18)$$

Upon evaluation of the integral and simplification of the result this control modal force equation can be shown that to be the same as derived by Dimitriadis et al. [14]:

$$U_n = M_o \left[-\frac{\gamma_x^2 \gamma_y^2}{\gamma_x \gamma_y} \right] (\cos(\gamma_x x_1) - \cos(\gamma_x x_2)) (\cos(\gamma_y y_1) - \cos(\gamma_y y_2)) \quad (4.19)$$

If in equation (4.15) the following substitutions are made:

$$\frac{\partial \phi(x,y)}{\partial x} = R_y(x,y) \quad \frac{\partial \phi(x,y)}{\partial y} = R_x(x,y) \quad (4.20)$$

the following equation is obtained:

$$U_n = \int_{x_1}^{x_2} R_x(x,y_1) M_o \, dx - \int_{x_1}^{x_2} R_x(x,y_2) M_o \, dx + \int_{y_1}^{y_2} R_y(x_1,y) M_o \, dy - \int_{y_1}^{y_2} R_y(x_2,y) M_o \, dy \quad (4.21)$$

upon evaluating this integral we are left with equation (4.10).

The line moment can be converted to the voltage necessary to drive the actuator pair by the following linear relationship:

$$\varepsilon_{pe} = \frac{M_o}{C_o} = \frac{d_{31} V^s}{t} \quad (4.22)$$

whose constants are defined in Chapter 2 in equations (2.6) through (2.9).

Similar to the point force model, the piezo can be modeled by a finite element forced response solution. The piezoelectric control actuator is modeled by applying line moments as the forcing function at each of its edges [14]. Due to the grid size of the finite element mesh, the length of the piezo spans three nodes. Therefore each edge line moment is modeled as three equivalent moments acting at the corresponding node in the direction corresponding to that shown in Figure 4.1, as

modeled by:

$$M_x = \frac{U_{ni} L_{px}}{3} \quad M_y = \frac{U_{ni} L_{py}}{3} \quad (4.23)$$

where L_{px} and L_{py} are the lengths of the piezo in the X and Y direction.

4.2 Boundary Element Model

This section will discuss a boundary element model using SYSNOISE versions 4.4ap and 5.0. SYSNOISE stands for System for Numerical Noise Analysis and is tailored to numerical modelling of acoustic fields in one, two, and three dimensions. SYSNOISE is capable of performing analysis using both finite element and boundary element methods in both closed and open regions. Having developed the above finite element model in CAEDS, SYSNOISE will be used solely for boundary element analysis. The boundary element method is formulated by applying Green's theorem to the Helmholtz equation. Using Green's theorem, a three dimensional problem with a volume integral is reduced to a two dimensional surface. Therefore it becomes necessary to discretize only the radiating surface rather than the surface and the surrounding media [30]. By using information from the finite element model, this model will be used to obtain the pressure at strategically located far field points discussed further in the next

section. This information will then be used to form the objective function, total radiated sound power.

For this boundary element model some preliminary options must be chosen. Sysnoise is capable of performing both finite element and boundary element analysis. Having developed the above finite element model in Caeds, Sysnoise will be used solely for boundary element analysis. The next option provides a choice between the collocation and the variational boundary element method. The collocation method, which is used in this model, is only available for the boundary element method, while the finite element method is capable of using either the collocation or the variational method. Other available options include interior or exterior, coupled or uncoupled, and baffled or unbaffled. This model assumes that there is little or no fluid loading on the structure, thus the system is uncoupled. This scenario can also be called pure acoustic modeling or one way coupling. This is a valid assumption considering the relative densities of air and steel. This model will be using the baffled option in which the structure is built in to an infinite baffle in the X-Y plane, separating the sound field into two sections. With this set of options the Rayleigh method is invoked for calculating the far field pressure, as was used in previous models [31].

To create the boundary element model it is possible to read in the mesh from the

"universal" or output file from the finite element model. The Sysnoise command "fmaximum" should then be executed, which determines the maximum frequency that can be studied with the mesh physical properties, using a default of six elements per wavelength [31]. For this case the maximum frequency was more than twice the frequency of the highest included natural mode and about five times the primary disturbance or excitation frequency.

For this formulation, it is necessary to solve for the pressure at the far field points due to the natural mode shapes. This quantity will be represented as P_n and will be incorporated into the far field pressure equation (4.27) in the next section. The procedure for calculating this pressure P_n is as follows. Sysnoise reads in a mode shape and generates a velocity file by multiplying the displacements by $j\omega$. Sysnoise is then given a response frequency for which it calculates a response and creates a "potential" file. This potential file consists of the surface pressure, velocity and intensity of the structure. This step also calculates the radiation efficiency by means of a ratio of the output and input power. The input power is formulated as the power radiated by an equivalent piston as follows [31]:

$$w_i = \rho c S \langle v_{rms}^2 \rangle \quad (4.24)$$

and the output or radiated power is formed as [31]:

$$w_o = \frac{1}{2} \int_s \text{Re}(pv^*) dS \quad (4.25)$$

with a radiation efficiency as follows [31]:

$$\sigma = \frac{w_o}{w_i} \quad (4.26)$$

where:

S = the surface area of the plate

v = the rms particle velocity at the plate surface

p = the pressure at the plate surface

The next step is to calculate the pressure at the field points due to this mode shape. In this calculation, the first step is to search or read this potential file such that the most recent file is used. The point mesh command is used which allows Sysnoise to interface with an external database, the hemisphere of field points. The post processing of field points is performed, which incorporates the Rayleigh integral to predict the far field pressure, and the results are written to an output file. The results consist of the pressure, velocity, and intensity at the far field points.

For directly calculating the far field pressure at the field points, a similar procedure

can be used. The method for the boundary element solution is the same as that above except that the nodal displacements are calculated from a forced response solution of the finite element model, instead of from the natural mode shapes. This is done for verification purposes and is discussed further in Chapter 6.

4.2.1 Objective Function

The objective function for this numerical model is the total radiated sound power as formulated in Chapter 2 where the integral equation (2.14) is reduced to the summation equation (2.15). The hemisphere of field points for this model is made up of 33 points, as shown in Figure 4.2. Twenty-five of these points actually make up the hemisphere while the other eight lie in between the existing points along one arc of the hemisphere to create a smoother, more accurate directivity pattern in the X-Z plane. For clarity a top view of the hemispherical field point mesh is shown in Figure 4.3. Take note that the coordinate system in Figure 4.3 has been transformed to the lower left edge of the plate as in Figure 2.1, which is shown to give a relative size between the plate and the hemisphere. To generate this mesh an arc was created every 60 degrees about the Z axis. Starting from the X-Y plane and proceeding along this arc toward the Z axis, a field point was created every eighteen degrees. The actual coordinates of each of the field points corresponding to the coordinate system in Figure 4.3 are tabulated in Table 4.1. The pressure at

the individual field points can be formed by the following equation:

$$P(\omega) = \sum_{n=1}^N (Ff_n + \sum_{i=1}^{Na} U_n M_i) P_n(\omega) H_n(\omega) \exp(j\omega t) \quad (4.27)$$

In calculating the total radiated sound power, the pressure at each of the twenty-five field points is weighted by its corresponding area, as tabulated in Table 4.1. These areas were formed by drawing arcs between the six arcs that the field points lie on. Circles parallel to the X-Y plane were also formed about these arcs between the field points as determined above by degree as proceeding along the cord from the X-Y plane toward the Z axis. Each of the twenty-five points is now enclosed in a bordered section of the surface area of the hemisphere. The new objective function is formulated as before in equation (2.15) but the field point pressures are now weighted by the area they represent as follows:

$$\Psi = \sum_{i=1}^I |p_i(R_i, \theta_i, \phi_i)|^2 A_i \quad (4.28)$$

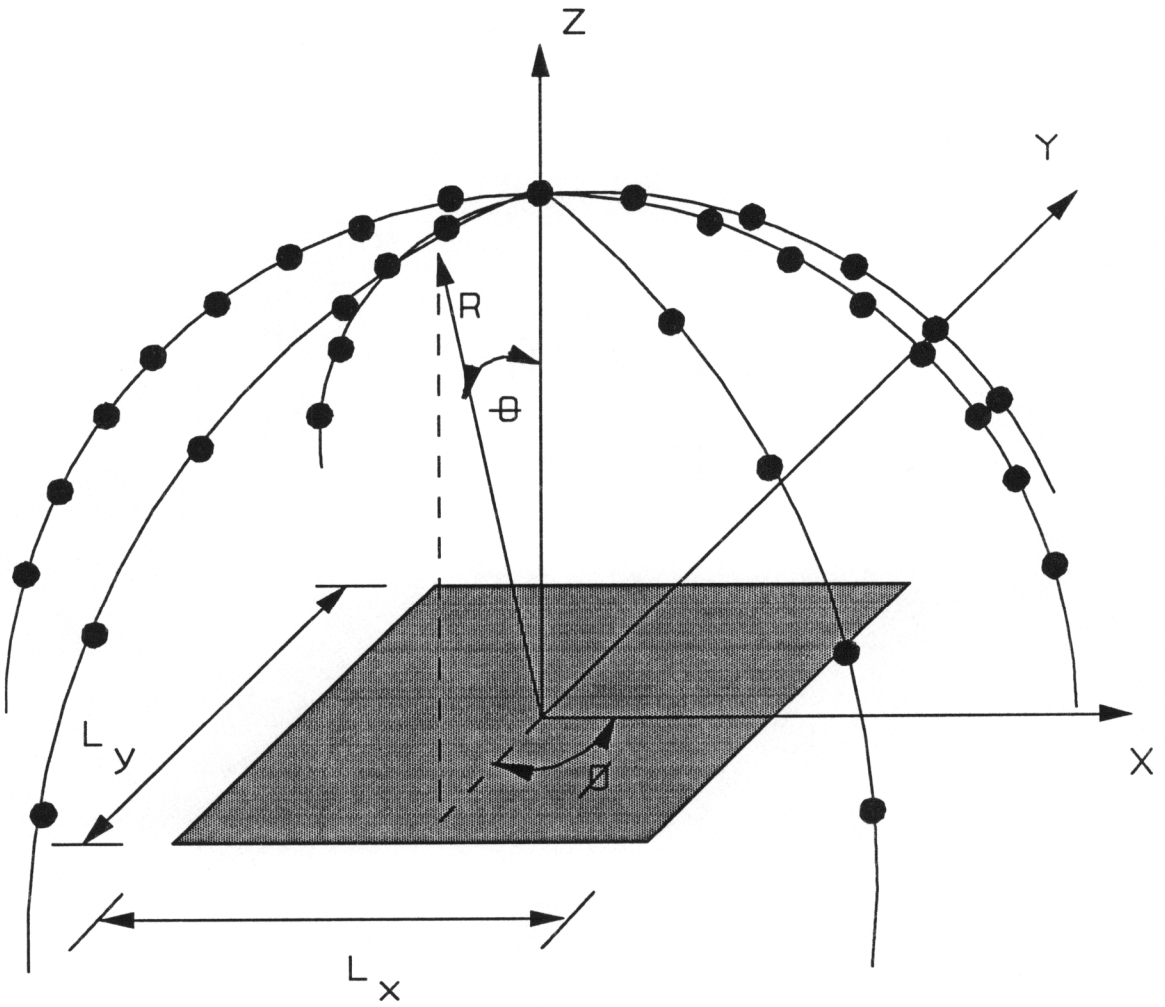


Figure 4.2: Objective Function Field Points

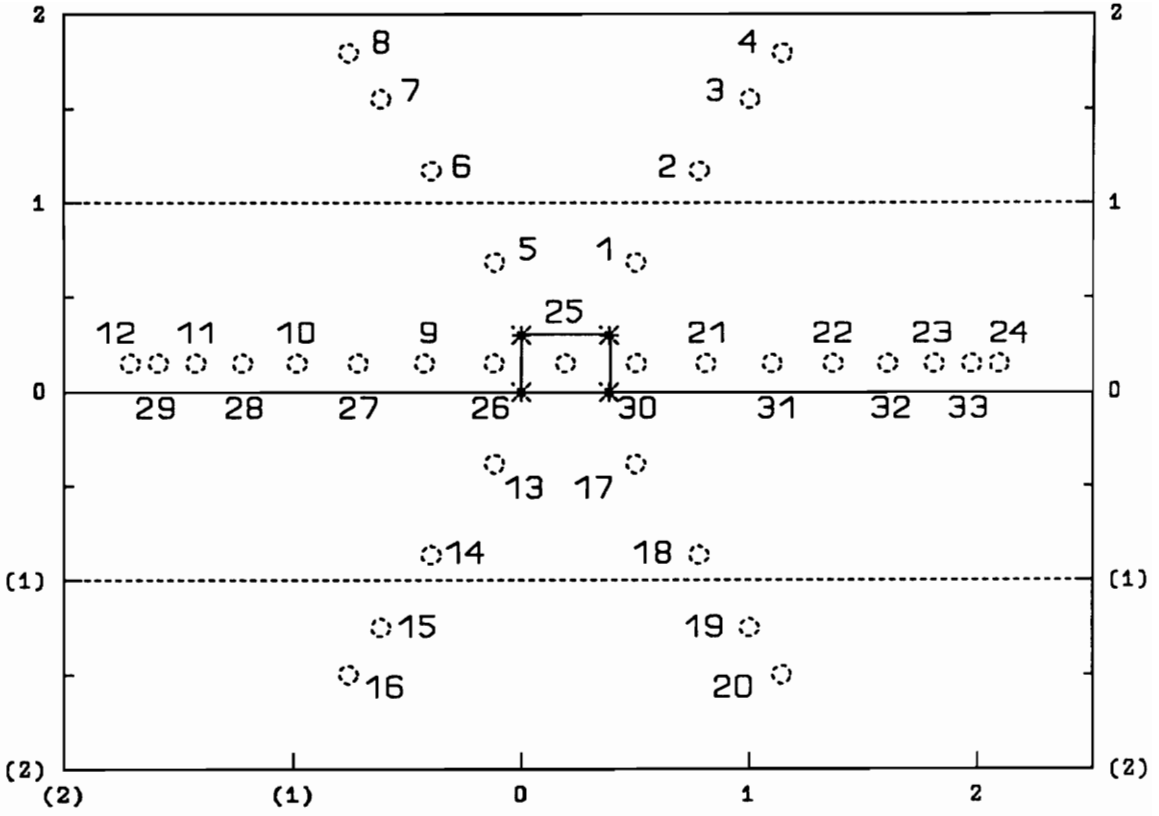


Figure 4.3: Top View of Hemisphere

Table 4.1: Field Point Coordinates

Point Number	Weight by Area	X Coordinate	Y Coordinate	Z Coordinate
1	.405	.4990	.6852	1.9021
2	.77	.7778	1.1681	1.6180
3	1.06	.9990	1.5513	1.1756
4	1.9	.1141	1.7973	.6180
5	.405	-.1190	.6852	1.9021
6	.77	-.3978	.1168	1.6180
7	1.06	-.6190	1.5513	1.1756
8	1.9	-.7611	1.7973	.6180
9	.405	-.4280	.1500	1.9021
10	.77	-.9856	.1500	1.6180
11	1.06	-1.4280	.1500	1.1756
12	1.9	-1.7121	.1500	.6180
13	.405	-.1190	-.3852	1.9021
14	.77	-.3978	-.8681	1.6180
15	1.06	-.6190	-1.2513	1.1756
16	1.9	-.7611	-1.4973	.6180
17	.405	.4990	-.3852	1.9021
18	.77	.7778	-.8681	1.6180
19	1.06	.9990	-1.2513	1.1756
20	1.9	1.1411	-1.4973	.6180
21	.405	.8080	.1500	1.9021
22	.77	1.3656	.1500	1.6180
23	1.06	1.8080	.1500	1.1756
24	1.9	2.0921	.1500	.6180
25	.309	.1900	.1500	2.000
26	-	-.1229	.1500	1.9754
27	-	-.7180	.1500	1.7820
28	-	-1.2242	.1500	1.4142
29	-	-1.5920	.1500	.9080
30	-	.5029	.1500	1.9754
31	-	1.0980	.1500	1.7820
32	-	1.6042	.1500	1.4142
33	-	1.9720	.1500	.9080

Chapter 5

Control and Optimization Approach

In order to minimize the objective function, the control actuator location and force must be optimized "simultaneously," as discussed later under the nonlinear optimization section. This control actuator has fixed dimensions for reasons discussed below. This section will develop the control and optimization approach used to find the optimal control forces and locations for multiple actuators. A cost function will be developed. The minimum of this quadratic function leads to the optimal actuator control forces for that particular actuator location. The objective function is then evaluated using these control forces at the corresponding location. A nonlinear optimization procedure is used to minimize the objective function which determines the optimal actuator locations. The optimization theory for the control force will be developed first, followed by the procedure for locating the optimal control location. However, before discussing the optimization procedures and/or algorithms, design variables and physical constraints must be considered.

5.1 Design Variables and Physical Constraints

For this study the size of the control actuator is not optimized due to practical limitations. An excessive voltage is required to drive the actuator as its size

decreases, invoking a constraint on the minimum size. The size of commercially available materials, as dictated by practical manufacturing of PZT material, sets a constraint on the upper dimension. For this study the PZT control actuator dimensions are fixed to be 38 x 31.5 x .2 mm. Figure 5.1 shows a schematic of the plate configured with a single PZT actuator pair. For this study these actuators will always be mounted in pairs as discussed in Chapter 2 and shown in Figure 2.2. As shown, the dimensions of the PZT actuator in the X and Y direction are denoted as w_{x_i} and w_{y_i} respectively. The spatial coordinates locating the center of the actuator are denoted as x_i and y_i with respect to the X and Y axis .

The design parameters are constrained by several physical limitations. One such limitation is the dimensions of the plate; i.e., the actuator must be constrained within the physical boundaries of the plate. In the case of multiple actuators, the design parameters must be constrained such as to prevent overlap of actuators. Based on work done by Clark in finding the point of actuator failure with similar parameters, the control voltage was limited to 400 volts peak to peak [32]. The mathematical formulations defining these constraints are discussed below.

The following set of equations constrain the PZT actuators within the plate boundaries:

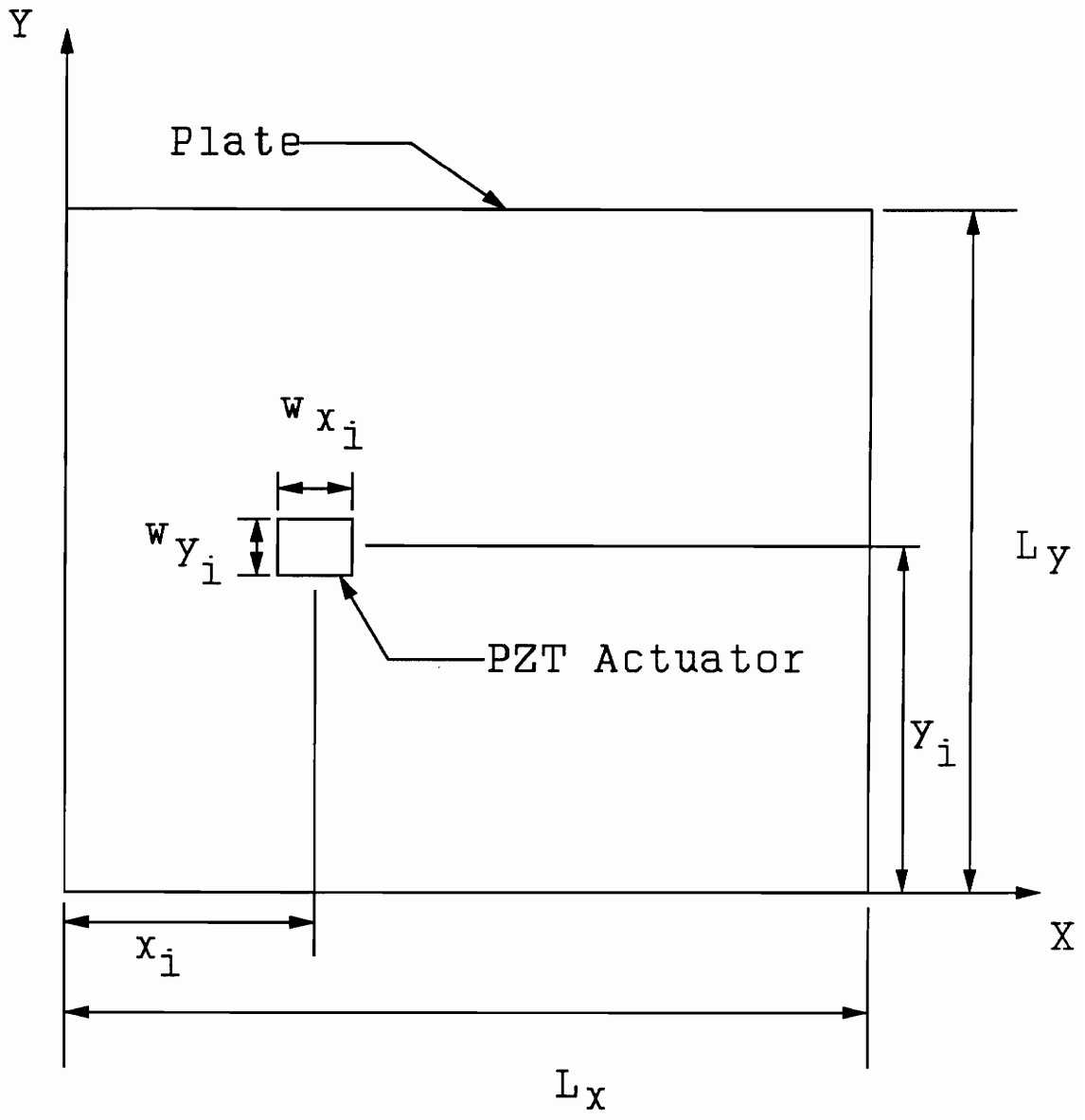


Figure 5.1: Schematic Of Plate Configured With A Single PZT

$$\begin{aligned}
x_{a_i} - w_{x_i} / 2 &\geq 0 \\
x_{a_i} + w_{x_i} / 2 &\leq L_x \\
y_{a_i} - w_{y_i} / 2 &\geq 0 \\
y_{a_i} + w_{y_i} / 2 &\leq L_y
\end{aligned}
\tag{5.1}$$

When implementing multiple actuators they must be constrained from overlapping. This can be done by forcing the distance between the center of the two actuators to be greater than two times the distance from the center of the actuator to the corner of the piezo patch, which can be achieved by the following equation:

$$\begin{aligned}
&[(x_{a_{(i+1)}} - x_{a_i})^2 + (y_{a_{(i+1)}} - y_{a_i})^2]^{\frac{1}{2}} - \frac{1}{2}[(w_{x_{a_i}}^2 + w_{y_{a_i}}^2)^{\frac{1}{2}} \\
&+ (w_{x_{a_{(i+1)}}}^2 + w_{y_{a_{(i+1)}}}^2)^{\frac{1}{2}}] > 0
\end{aligned}
\tag{5.2}$$

A physical constraint is also required on the complex control voltage of PZT actuator:

$$[V_{a_i}] \leq 400 \quad (\text{volt p-p}) \tag{5.3}$$

5.2 Linear Quadratic Optimal Control Theory

The objective here is to apply a minimization technique to a quadratic function, the cost function shown in equation (4.28), which is similar to the quadratic

function developed by Lester and Fuller [33]. Linear quadratic optimal control theory (LQOCT) is one such minimization technique that can be used when any type of external control source is applied to a structure. LQOCT is used to solve for the optimal control actuator forces with respect to the necessary complex voltage, or linearly related line moment as shown in equation (4.22), applied to its edges. These line moments induce pure bending moments on the plate which provide the structural control input necessary to achieve the control of the total radiated sound power.

The cost function represents the quantity to be minimized, which is the sum of the squares of the response at each of the error sensors, or field points in this study, as weighted by their corresponding areas discussed in the previous chapter:

$$C = \sum_{b=1}^{N_e} e_b e_b^* A_b \tag{5.4}$$

where:

e_b = the output of error sensor

e_b^* = the complex conjugate of e_b

A_b = the corresponding area

N_e = the number of error sensors (25)

The error sensor can be modeled with the transfer functions between the sensor

and both the disturbance and the control actuators, as follows:

$$e_b = \left(\sum_{s=1}^{N_a} T_{bs} M_s \right) + T_{bD} F \quad (5.5)$$

where:

T_{bs} = the transfer function between the S^{th} actuator and the b^{th} error sensor

T_{bD} = the transfer function between the disturbance and the b^{th} error sensor

M_s = complex moment for the S^{th} actuator

F = the input force

N_a = the number of actuators

To proceed with the solution, take the partial derivative of equation (5.4) with respect to the real and imaginary part of each control input, represented in equation (5.5), and equate each expression to zero. This operation leads to a system of equations that can be expressed in general form as:

$$\left(\sum_{b=1}^{N_e} \left(\sum_{l=1}^{N_a} T_{bl} M_l + T_{bD} F \right) T_{bs}^* = 0 \right) \quad (5.6)$$

Because the cost function is forced to have zero slope, the solution to the above system of equations yields the optimal control inputs. Equation (5.6) can be represented with linear algebra as follows:

$$[A]\{M\}=[b] \quad (5.7)$$

The above equation may be solved by inverting the [A] matrix and multiplying it by the [b] matrix; however, this may not be the most computational stable solution. In this work the above system of equations is solved by an IMSL subroutine called DLSACG. This algorithm first uses IMSL subroutine LFCCG to compute an LU factorization of the coefficient matrix and to estimate the condition number of the matrix. The solution of the linear system is then found using an iterative refinement routine LFICG. DLSACG also checks to see that [A] is not singular or close to singular. The routine also gives a warning if the condition number is greater than $1/\epsilon$ where ϵ is the machine precision. This condition would demonstrate the properties such that a very small change in [A] could cause a very large change in the solution vector {M} [34].

5.3 Nonlinear Optimization

It has been shown in previous studies by Clark and Fuller that increasing the number of control channels results in an increase in the far field attenuation [16, 35]. However, in terms of practical implementation, only a low number, about ten or less, of control channels are feasible with the present control strategies. It has also been shown that having prior knowledge of the structural modes which

contribute to the radiated sound can significantly reduce the number of necessary control channels.

Finding the optimal actuator locations is a significant problem. The general idea is to use a gradient search of the objective function in order to find its minimum, which corresponds to the optimal actuator location. In order to invoke this gradient search an actuator must be placed on the plate surface and then LQOCT is used to find the optimal control force for that actuator location. The initial location is then updated in the predicted direction of negatively increasing slope of the objective function, and another iteration of the procedure is made until the solution criteria is met. This method lends itself to several problems. Not knowing the complexity of the shape of the objective function, this method is only as good as the initial "guess" at the optimal actuator location. If the objective function is particularly complex, what seems to be a minimum from the algorithm's standpoint may only be a local minimum or sub-optimal solution and far from the actual minimum or optimal solution, both in location and achievable attenuation.

An approach to combat this problem is to divide the plate into quadrants and locate an actuator in the center of each of the quadrants. This method then becomes more accurate as the size of the quadrants decrease, and approaches the computational intensive brute force method of trying every possible location of

a control actuator. This method demonstrates the tradeoff between accuracy of solution and computational effort.

For this approach, it was decided to incorporate both methods, using the quadrant method to learn enough about the objective function to make educated guesses or target locations to implement the gradient search method. The plate was first traversed with a piezo patch at many locations on the plate such that there was very little overlap of areas previously covered by other actuator locations. This corresponds to a grid of 117 points, having three centimeters between the center coordinates of potential actuator locations. Minimizing the cost function for each of these possible locations, an objective function can be plotted to observe the difficulty of the location optimization. A plot of the objective function for optimizing a single actuator on the plate is shown in Figure 7.3. The Z axis of this is the total radiated sound power before it is converted to the dB scale. Having seen this objective function, one can get an accurate estimate of where the local minima or sub-optimal solutions are. These estimates can then be used as target locations for the gradient search algorithm, used to find the optimal solution.

5.4 Review of IMSL Codes

The optimization algorithm chosen for this study is an IMSL subroutine called

DNOONF which solves a general nonlinear programming problem [34]. Within this successive quadratic programming algorithm, the gradient of the design parameters is estimated by another IMSL subroutine, DCDGRD, by means of the central finite difference method [34]. The constrained optimization problem can be expressed mathematically by the objective function [36]:

$$\min_{x \in \mathbb{R}^n} f(x) \tag{5.8}$$

subject to the equality constraints:

$$g_j(x) = 0, \text{ for } j=1, \dots, m_e \tag{5.9}$$

and the inequality constraints:

$$g_j(x) \geq 0, \text{ for } j=m_e+1, \dots, m \tag{5.10}$$

$$x_l \leq x \leq x_u$$

where m_e is the number of equality constraints, m is the total number of constraints, and all problem functions are assumed to be continuously differentiable. The solution technique is based on the iterative formulation and solution of quadratic programming subproblems. These subproblems are obtained by using a quadratic approximation of the Lagrangian and by linearizing the

constraints as:

$$\min_{d \in \mathbb{R}^n} \frac{1}{2} d^T B_k + \nabla f(x_k)^T d \quad (5.11)$$

subject to:

$$\begin{aligned} \nabla g_j(x_k)^T d + g_j(x_k) &= 0, \quad \text{for } j=1, \dots, m_e \\ \nabla g_j(x_k)^T d + g_j(x_k) &\geq 0, \quad \text{for } j=m_e+1, \dots, m \\ x_l - x_k &\leq d \leq x_u - x_k \end{aligned} \quad (5.12)$$

where B_k is a positive definite approximation of the Hessian, and x_k is the current iterate. Let d_k be the solution of the subproblem. A line search is used to find a new point x_{k+1} [34],

$$x_{k+1} = x_k + \lambda d_k, \quad \lambda \in (0, 1] \quad (5.13)$$

such that a 'merit function' will have a lower function value at the new point. Here the augmented Lagrangian function is used as the merit function [37]. The iteration process continues and updates the design parameters until the accuracy criteria is satisfied [34].

Within this nonlinear optimization algorithm it should be noted that with each iteration of the actuator location, the control voltage must be optimized, using

LQOCT as discussed above. Optimization of multiple actuators is achieved by an iterative means of the procedure used for the optimization of a single actuator. After finding the optimal location for a single actuator, the actuator is fixed at that location while the plate is traversed by a second actuator. The data from this traverse is used to generate a plot of the new cost function, as shown in Figure 7.4. This plot shows the new sub-optimal actuator locations which are used as targets along with the single optimally located actuator coordinates. The gradient search algorithm is reinstated with both actuators free to move as dictated by the algorithm. It was observed that the location of the optimal solution for the single actuator case changes only slightly with the addition of a second actuator.

One of the original goals of this project was to increase the speed of the optimization procedure. It was thought the algorithm could be given the number of multiple actuators and allowed to solve for their optimal locations efficiently. This is a possible method; however, after seeing the shape of the objective functions, it is obvious that this type of algorithm would have trouble finding the optimal solution. There are so many sub-optimal solutions for the algorithm to get caught in that converging on the optimal solution without using the method developed above is highly unlikely.

Even with good targets the method often takes several hours to converge on a

solution using the VTVM1 mainframe. For this reason it is very helpful to first traverse the plate to find good targets for potential actuator locations. The step size of the traverse was again a tradeoff between accuracy and computational efficiency. A step size of three centimeters turned out to be a good choice. The plate could be traversed in slightly over an hour and the accuracy of the solution was typically only improved slightly by the use of the gradient search technique. The convergence time of this gradient search algorithm was decreased significantly by having the prior knowledge of the objective function from the traverse data.

Chapter 6

Model Verification

Before a parametric study can be done using this numerical model, the model must be verified for accuracy. This verification will begin with the modeling of a simple structure; a simply supported flat plate in an infinite baffle driven by a pure tone, off resonance, primary point force. The solutions of the three previously developed models will be compared. For this comparison the structure was excited by a point force at the coordinates (.240, .124). This is the same location used by Clark to avoid node lines of the first twenty-five mode shapes [9]. The excitation force was of unit magnitude at an off resonance frequency of 550 Hz.

For a stiff, homogeneous panel flexural waves propagate along its surface at a particular frequency. Since the propagation is dispersive there exists a critical frequency at which the wavelength of the flexural or bending wave equals that of a wave of the same frequency in air. The critical frequency, f_c , can be calculated using the dimensions and material properties discussed in Chapter 2 by use of the following equation [38]:

$$f_c = \frac{\sqrt{3}c^2}{\pi h} \sqrt{\frac{\rho}{E}} \quad (6.1)$$

Wallace found that just below the critical frequency there exists a certain waviness in the radiation efficiency curves of the higher mode numbers due to the appearance of grazing incidence of new radiation lobes. Just above the critical frequency the radiation efficiency curves display a peak, the height of which increases with mode number. In the region of wave coincidence, well above the critical frequency, the radiation efficiency curves asymptotically approach unity [23]. For the plate in this study the critical frequency is 6429 Hz, well above the excitation frequency of 550 Hz.

6.1 Simple Structure

The natural frequencies as solved for in the three models are extremely close and are tabulated in Table 6.1. The directivity patterns, defined as the hypothetical surface in space over which the sound pressure levels produced by the source are constant [2], are calculated by the far field pressure equations developed in the various models. These pressures were evaluated at the far field points in the X-Z plane at $Y = Y/2$ of the plate at a radius of two meters. The directivity patterns for the analytical, assumed modes, and numerical model also compare well, and are

shown in Figure 6.1. The coordinate system shown in this directivity pattern may be associated with the objective function coordinate system shown in Figure 2.3, where negative theta corresponds to increasing theta from the Z axis towards the negative X axis where phi equals 180° , and positive theta corresponds to increasing theta from the Z axis to the X axis where phi equals zero. As can be seen, the directivity patterns calculated by these three models are almost identical. The analytical model (1) and the assumed modes analytical model (2) directivity patterns differ by .07 dB at the field point of maximum deviation. The field point pressure as predicted by the numerical model is approximately 1 dB lower than that predicted by the analytical model. Some of this difference is due to the fact that there are a different number of modes used in the models. The analytical model uses the first sixteen modes while the assumed modes model and the numerical model use only the first eleven modes, as tabulated in Table 3.1. This implies that the modes higher in frequency than the first eleven modes do not contribute significantly to the directivity pattern.

To investigate this, the analytical model was used to compute the directivity pattern taking into account the first twenty five modes, and is plotted with the sixteen mode directivity pattern in Figure 6.2. The difference in the field point pressure at the maximum deviation between the 16 mode solution (1) and the 25 mode solution (2) was .6 dB. The difference in the total radiated sound power between

Table 6.1: Natural Frequencies

Mode	Analytical	Assumed Modes	Numerical
1	86	86	86
2	185	185	185
3	245	245	245
4	344	344	342
5	350	350	351
6	509	509	504
7	510	510	513
8	581	581	587
9	609	609	606
10	740	740	735
11	774	774	762

these two models was .4 dB. The total radiated sound power for the 16 mode solution was 72.86 dB, and was found by using the Simpson's rule to integrate over the hemisphere at a radius of 2 meters from the center of the plate. With the formulation reducing the integral to a summation, used to develop equation (4.28), the total radiated sound power as predicted by the numerical model was 80 dB. The sound power calculated by the analytical model, also using this formulation as shown in equation (2.15), is also higher than evaluating the integral, but only uses about a third of the number of field points used by the numerical model. The sound

power calculated by this formulation of reducing the integral to a summation is significantly higher in both cases than that found by evaluating the integral. Because the pressure at the far field points agree extremely well between the various models, the difference in the total radiated sound power must be attributed to the formulation of reducing the integral to a summation, and the number of far field points used to evaluate the summation.

A finite element forced response calculation, as discussed in Chapter 4, was also performed for further verification of the above numerical model. This calculation was also done using the first eleven modes. The directivity pattern for the numerical model and the forced response numerical model are shown in Figure 6.3. The directivity patterns for the numerical model (1) and the forced response numerical model (2) compare well, differing by only .4 dB at its point of maximum deviation, zero degrees.

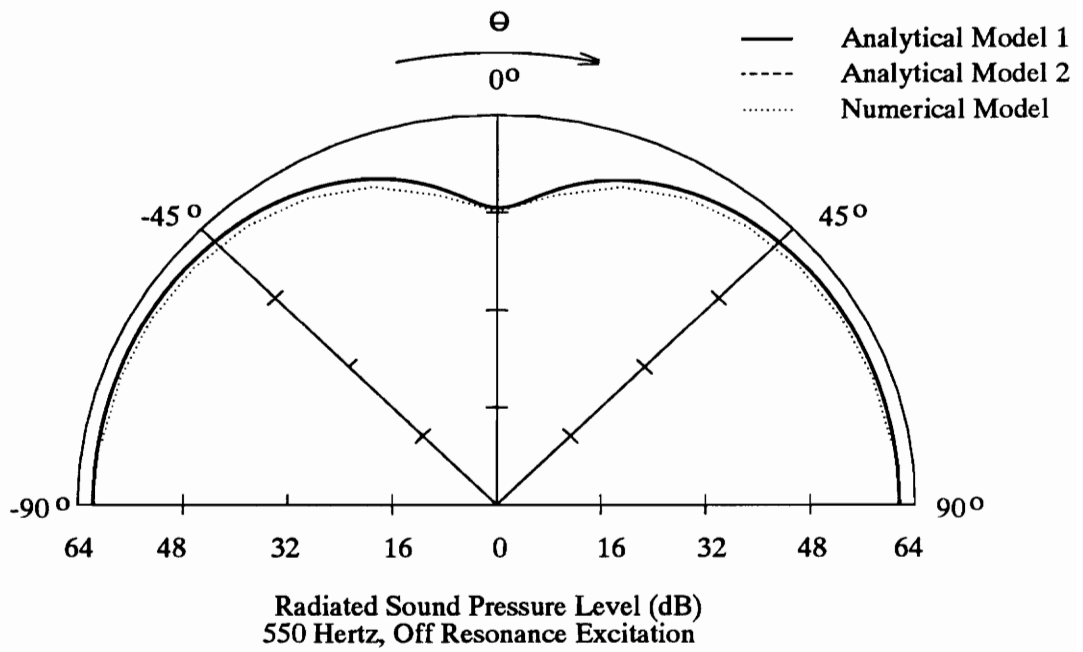


Figure 6.1: Directivity Patterns For Simple Structure Model Verification

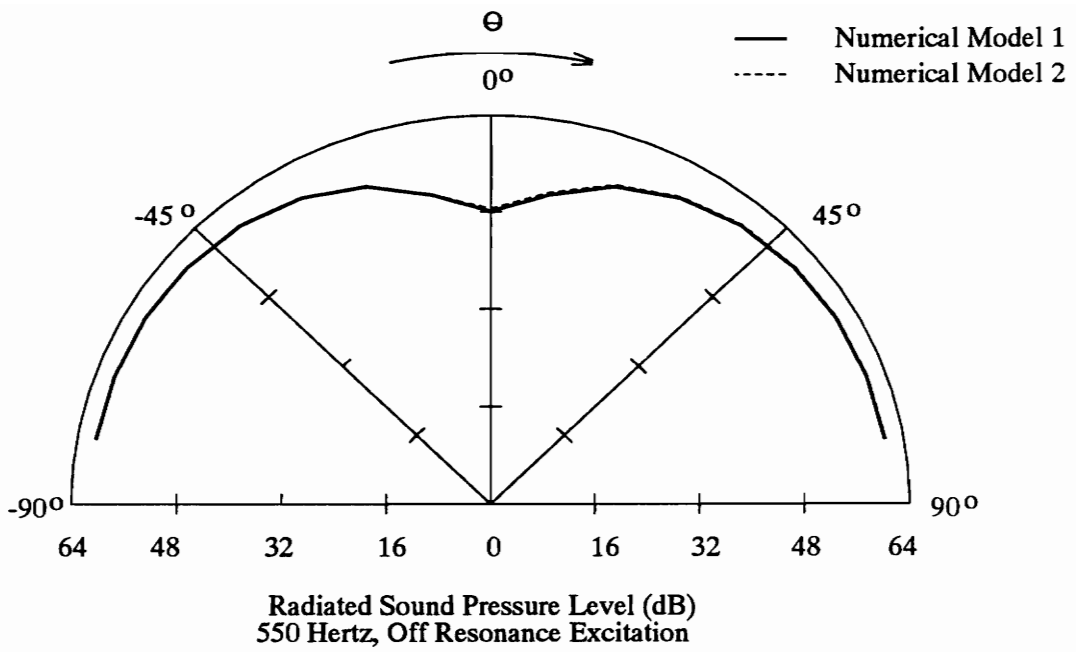


Figure 6.3: Directivity Pattern For Simple Structure Numerical Model Verification

6.2 Complex Structures

Having shown that the results of the various models of the simple structure compare very well, complex structures may now be examined. The first complex structure modeled was a simply supported flat plate with a point mass at its center. This point mass was .1 kg, corresponding to about 6 percent of the total mass of the plate. The primary excitation is the same as that used in the previous section, and will be used throughout this work. This case was modeled using both the assumed modes method model and the numerical model.

There are several possible ways to model a point mass within the numerical model. One consideration is that due to the mesh configuration, there is not a node in the center of the plate. The Finite element software contains lumped mass elements; however, they must be applied at a node. Another node could be added and connected to the existing mesh but this procedure would lead to a nonuniform mesh and was therefore ruled out. A simple solution is to change the density of the center element to include the .1 kg point mass in addition to the density of that section of the plate. Yet another option is to divide the .1 kg point mass into four mass elements and apply one of them at each of the nodes of the element in the center of the plate. These two methods should be very similar when using the mass lumping formulation as discussed earlier in Chapter 4. Both of the methods

for modeling the point mass were implemented to find the most accurate modeling technique.

A rough estimate of the fundamental natural frequency for the plate with a point mass at the center can be calculated using the following equation [21]:

$$\omega_{m1}^2 = \frac{\omega_1^2}{1 + m_p \sqrt{\frac{4}{\rho'' L_x L_y}}} \quad (6.2)$$

where:

ω_{m1} = first natural frequency for plate with point mass

ω_1 = first natural frequency for plate without point mass

m_p = point mass (.1 kg)

The predicted frequency using this rule of thumb is 2 Hz higher than the fundamental frequency as calculated by the assumed modes method. The first eleven natural frequencies calculated by the assumed modes method model, the numerical model with the modified density element, and the numerical model with lumped mass elements, are shown in Table 6.2 and agree extremely well. The two numerical model solutions are identical to each other and differ by 7 Hz or less from the assumed modes model. As expected, the natural frequencies of the

modes in which the central mass was on a nodal line did not change in magnitude from the natural frequencies in the case with no mass. Because the mass was on a node line it was not seen by the mode shape, no energy was required to try to displace the point mass which would have caused a decrease in the natural frequency of that mode. The mode shapes with a node line in the center of the plate are the even-odd modes, the odd-even modes, and the even-even modes.

Table 6.2: Natural Frequencies With Center Mass

Mode	Assumed Modes	Numerical Density Element	Numerical Mass Element
1	77	77	77
2	185	184	184
3	245	244	244
4	311	318	318
5	344	341	341
6	474	477	477
7	509	502	502
8	581	579	579
9	609	605	605
10	710	710	710
11	740	734	734

The directivity patterns for the assumed modes model, the numerical model with

the modified mass density element (1), and the numerical model with the lumped mass elements (2), and the assumed modes analytical method model are shown in Figure 6.4. The maximum difference in pressure at any given field point between the two numerical model directivity patterns is .003 dB. The maximum pressure difference between any given field point in the assumed modes model and the mass element model is 1.1 dB. The total radiated sound power is identical as calculated by the two numerical models, and is consistently higher than that of the assumed modes method model as discussed in the previous section. The radiated sound power increased by 2 dB as compared to the plate without the point mass at the center.

As demonstrated by the example cases run, the numerical model is accurate as compared with the solutions of the assumed modes model for the complex structure of a simply supported flat plate with a point mass at its center. The numerical model is also accurate as compared with the solutions of the assumed modes model and the closed form analytical model for the simple structure. The only significant difference is in the total radiated sound power. This discrepancy has been accounted for in the previous section (6.1) and is consistent. It has been shown that the pressure at the field points as predicted by the numerical and analytical model agree very well, and the difference in the total radiated sound power is therefore attributed to the formulation. The rest of this study will be

concerned with sound power attenuation, or the reduction in the total radiated sound power due to active control and this discrepancy will therefore be insignificant. The same trends are seen when comparing the various models with applied control. The control was also modeled numerically and analytically for verification of the formulation. For the sake of completeness the response of the plate was compared for the various models and showed an even higher percentage of agreement.

Chapter 7

Point Mass Parametric Study

The numerical model has been shown to be accurate in the previous section and will now be used to study the effects of a point mass discontinuity on the surface of the structure. The point mass ranges from ten to twenty-five percent of the mass of the plate, in increments of five percent. One study was performed with the point mass at the center of the plate and another was done with the point mass off center at coordinates (.14, .176 m), which corresponds to node 208. For these 'case studies' the natural frequencies and mode shapes were examined for the first eleven modes of each point mass load case. For the fifteen, twenty, and twenty-five percent mass load cases, the directivity patterns were calculated along with the total radiated sound power. Control was also applied to these cases by locating the optimal actuator forces and locations for single and multiple actuator pairs. This data will be presented and from it some conclusions will be drawn and some trends will be developed. The data from the control applied to the simple structure will be presented first, followed by the centered point masses and then the off center point masses.

7.1 Simple Structure

The modal indices, natural frequencies, and radiation efficiencies of the simply supported flat plate excited by a 550 Hz off resonance point force are tabulated in Table 7.1. The radiation efficiency drops off sharply after mode three. Figure 7.1 shows the directivity pattern for the simply supported plate with no control, with optimally located single actuator pair, and with two optimally located actuator pairs (a double actuator pair). The directivity pattern before control has a distinctive notch at zero degrees due to the significant contribution of mode two which has a directivity pattern resembling that of a dipole source. The total radiated sound power before control is 80.74 dB.

The location for an optimally located single actuator pair are shown in Figure 7.2 as (1), along with the optimal locations for two control actuator pairs (2). Using one control actuator pair located at center coordinates (.146, .241) of the piezo patch, the total radiated sound power was attenuated by 8.2 dB. The corresponding directivity pattern is similar in shape to the before control case except that the notch has shifted slightly off center. This would infer that the node line of mode two was moved to the right due to the actuator placement. This directivity pattern demonstrates the characteristics of modal suppression in which the radiation distribution of all of the modes is suppressed by the control force. The objective

function used to locate the targets for this single actuator optimization can be seen in Figure 7.3. From this figure it can be seen that there are many targets, or sub-optimal solutions.

With two control actuator pairs located at center coordinates (.132, .248, and .0939, .216) the sound power was attenuated 18.5 dB. This directivity pattern has no notch at the center but has symmetrical notches just below 45 degrees, making it a 3 lobe directivity pattern. This directivity pattern implies modal restructuring in which the lower order response distribution is changed to higher order distribution with lower radiation efficiency. It should be noted that the single actuator pair moved only slightly when introducing a second actuator pair. The cost function for locating the second actuator pair as discussed in Chapter 5 can be seen in Figure 7.4 and is very different from the single actuator cost function.

Table 7.1: Simple Structure Solutions

Mode	X Index	Y Index	Natural Frequency (Hz)	Radiation Efficiency (σ)
1	1	1	86	.845
2	2	1	185	.260
3	1	2	245	.172
4	2	2	342	3.152E-2
5	3	1	351	4.843E-2
6	3	2	504	5.405E-2
7	1	3	513	1.242E-2
8	4	1	587	4.404E-2
9	2	3	606	2.085E-2
10	4	2	735	6.248E-3
11	3	3	762	2.948E-3

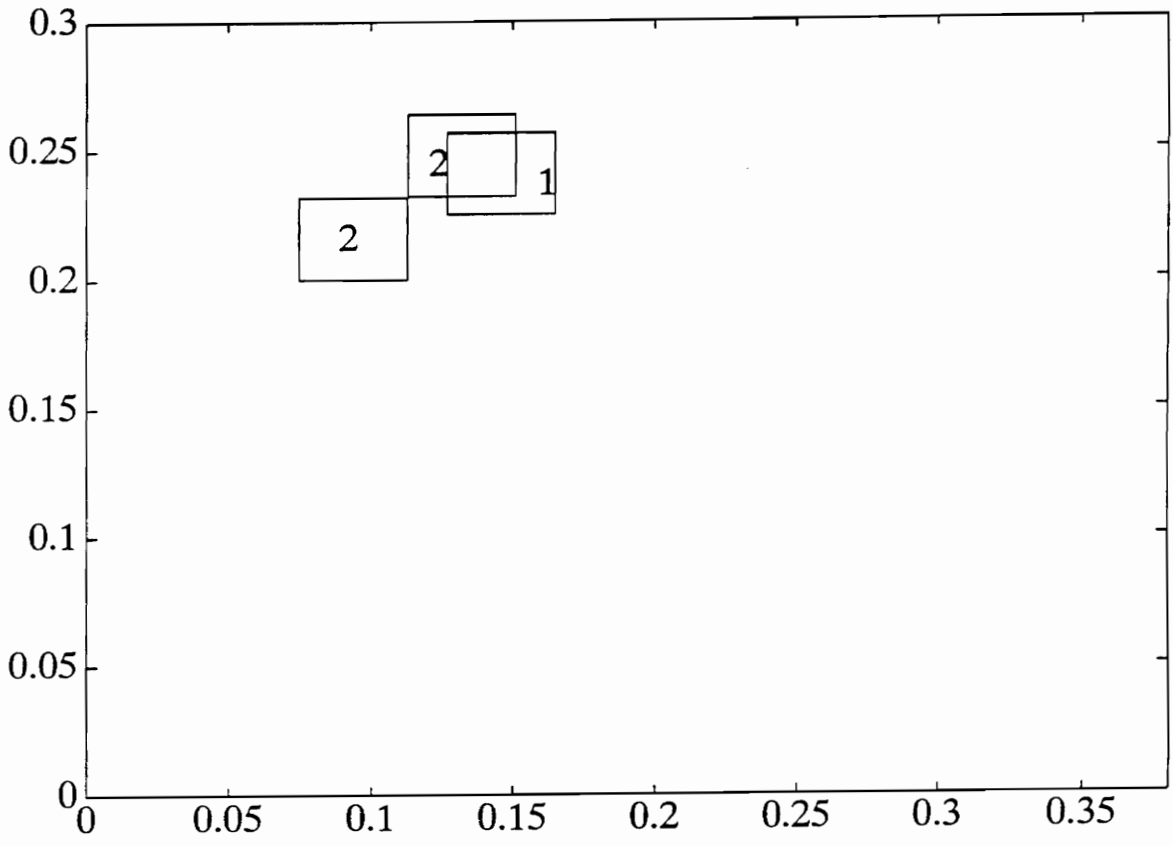


Figure 7.2: Control Actuator Locations For Simple Structure

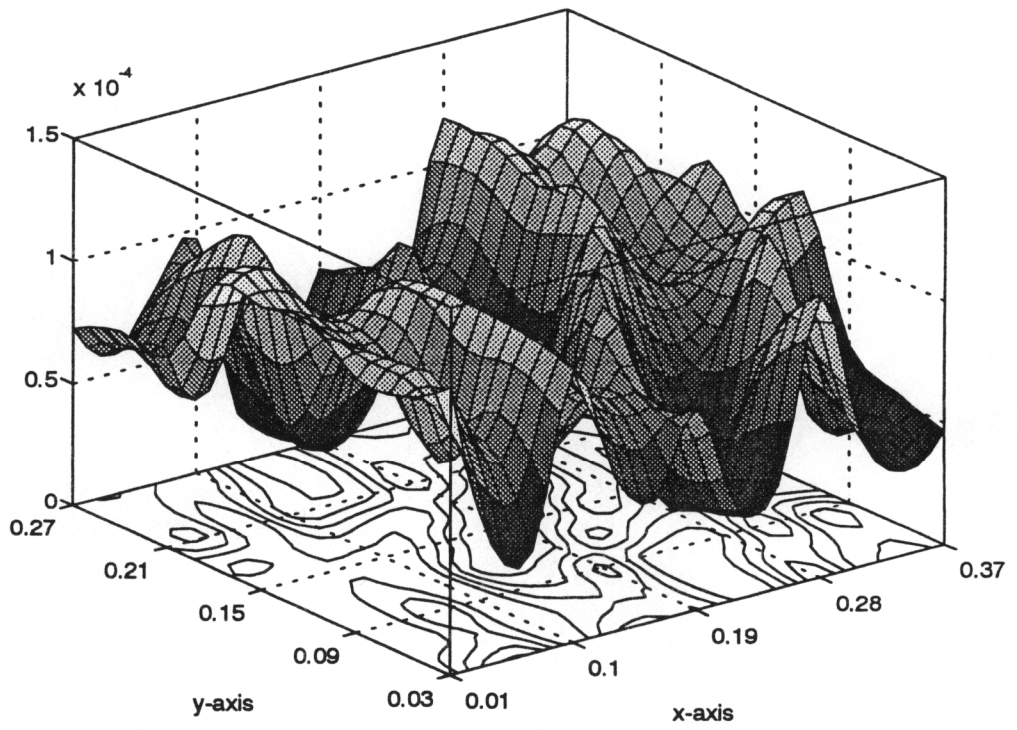


Figure 7.3: Objective Function For 1 PZT

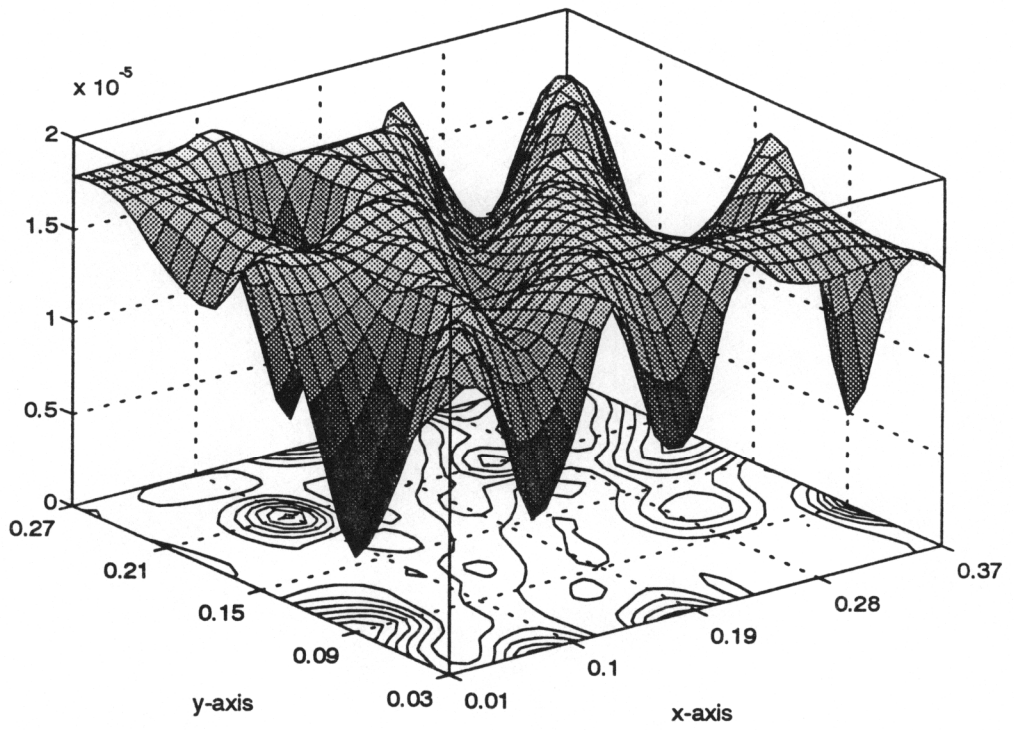


Figure 7.4: Objective Function For 2 PZTs

7.2 Centered Point Mass

This section will present data from a study of placing a point mass at the center of a simply supported plate driven by the primary disturbance of a 550 Hz point force. The point masses used in this study correspond to 10, 15, 20, and 25 percent of the plate mass, which is 1.72 kg. The modal indices and their corresponding natural frequencies are shown in Table 7.2. It should be noted that some of these mode shapes are deformed due to the point mass. When this is the case, the modal indices tabulated correspond to a normal mode shape that the deformed mode shape most closely resembles, and is marked with an asterisk.

As expected the fundamental frequency decreases with increasing mass. Ideally, the frequencies corresponding to the even-odd, the odd-even, and the even-even mode shapes should not change from the simple structure model because the mass is on a node line. Upon inspecting the results, with the point mass, the order in which the mode shapes occur is different from the simple structure, however the only frequencies that decrease significantly with increasing mass correspond to the odd-odd mode shapes with the exception of mode eight, the (4,1) mode.

The frequencies of the odd-odd mode shapes do change slightly with increasing mass due to the grid size of the finite element mesh. There is an element instead

of a node at the center of the plate, therefore a single lumped mass element cannot be located at the exact center. This leads to mass inertia loads which cause these slight changes in the frequencies of the odd-odd mode shapes. The most significant of these changes is noticed in mode eight. This is because the element is slightly larger in the X direction than in the Y direction, therefore having a greater mass inertia load with a higher modal index in the X direction.

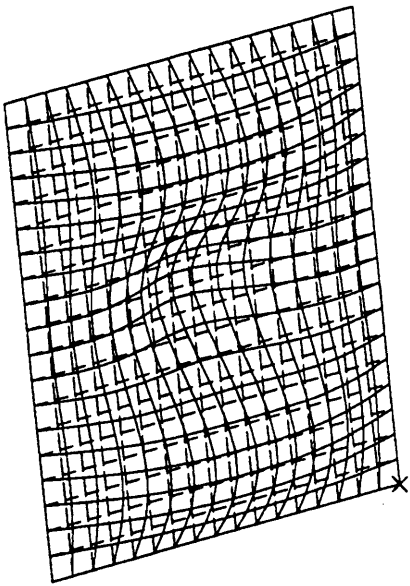
Table 7.2: Natural Frequencies With Center Mass

Mode	X Index	Y Index	10% Mass	15% Mass	20% Mass	25% Mass
1	1	1	73	68	64	60
2	2	1	184	183	183	182
3	1	2	242	243	242	241
4*	3	1	303	289	279	271
5	2	2	341	341	341	341
6*	1	3	467	459	455	452
7	3	2	501	499	497	495
8*	4	1	573	565	556	546
9	2	3	604	604	604	603
10*	3	3	656	685	679	675
11	4	2	734	734	733	733

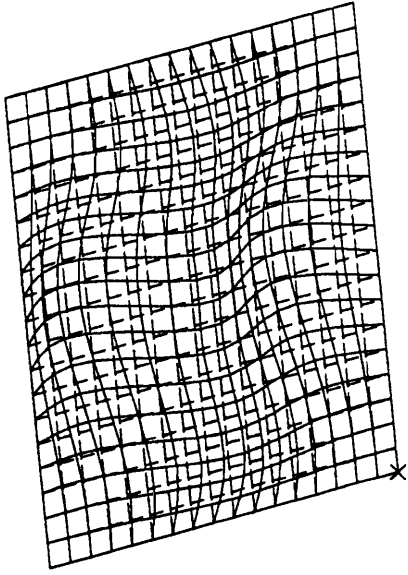
In addition to the changing frequencies of the odd-odd modes, the mode shapes also change significantly. The modes that changed shape the most were modes four, six, eight, and ten, which can be seen in Figure 7.5. Mode shape four has a greater net displacement than the typical (3,1) mode because of the induced damping in the upper and lower third of the center of the plate. although shapes six, eight, and ten are deformed, they still retain a similar degree of net displacement as without the mass, however more of this net displacement is near the edge of the plate.

The radiation efficiencies for each of the modes are tabulated in Table 7.3. The radiation efficiency of each mode is relatively constant with respect to the point mass except for modes four and modes nine. The radiation efficiency of mode four increases with increasing mass. This is because the deformed mode shape as can be seen in Figure 7.5 becomes more deformed with increasing mass, meaning that it has an increasing net displacement in one direction. The radiation efficiency drops off sharply after mode four for all point mass cases. This is due to the fact that the rest of the mode shapes above mode have little net displacement. The radiation efficiency of these deformed mode shapes is higher than the corresponding modes shapes of the plate without the point mass.

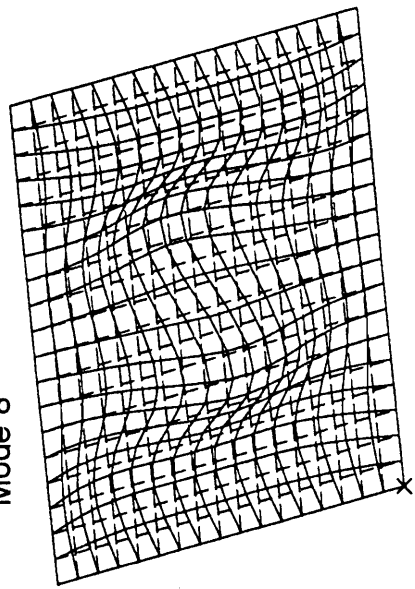
Mode 4



Mode 6



Mode 8



Mode 10

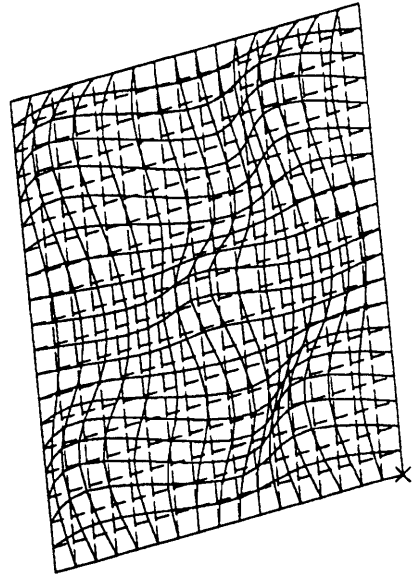


Figure 7.5: Deformed Modes With Center Mass

Table 7.3: Radiation Efficiencies With Center Mass

Mode	10% Mass	15% Mass	20% Mass	25% Mass
1	.837	.834	.832	.830
2	.259	.259	.259	.259
3	.171	.171	.171	.171
4	.277	.388	.469	.529
5	3.152E-2	3.151E-2	3.151E-2	3.151E-2
6	9.586E-2	9.678E-2	9.587E-2	9.456E-2
7	1.426E-2	1.542E-2	1.671E-2	1.815E-2
8	5.910E-2	6.491E-2	7.032E-2	7.579E-2
9	1.065E-2	8.260E-3	6.778E-3	5.808E-3
10	6.066E-3	6.484E-3	6.679E-3	6.740E-3
11	6.284E-3	6.304E-3	6.326E-3	6.348E-3

The directivity patterns for the fifteen, twenty, and twenty-five percent point mass models before and after control are shown in Figure 7.6, Figure 7.7, and Figure 7.8, respectively. The total radiated sound power before control and the sound power attenuation with a single and double actuator pair is shown in Table 7.4. From this data it can be seen that the sound power before control increases with mass. This is due mostly to the fact that the system is approaching resonance. It is also partly due to the increasing mode shape deformation with mass. Due largely to mode four, it can be seen that the net radiation efficiency

increases with mass. The notch in the directivity pattern grows deeper as the point mass increases. The amount of attenuation achievable with a single and a double actuator pair also increases with the increase in the point mass. The increase in attenuation gained by adding a second actuator ranges from roughly 4 to 13 dB. These increases however are at a diminishing rate. The data shows the sound power attenuation achievable with a double actuator pair starts to level off shortly after the mass exceeds twenty percent of the mass of the plate.

Table 7.4: Sound Power And Attenuation With Centered Mass

Centered Point Mass	Before Control Sound Power (dB)	Sound Power Attenuation 1 Pzt (dB)	Sound Power Attenuation 2 Pzts (dB)
15% Mass	87.12	19.2	31.8
20% Mass	94.85	30.1	40.0
25% Mass	97.73	36.6	40.5

The directivity pattern using one actuator for control has notches above positive and negative forty-five degrees. This implies modal restructuring of the lower order modes. This directivity pattern loses its minor lobes, but keeps its notches as the point mass increases. This is because the radiation efficiency of mode four

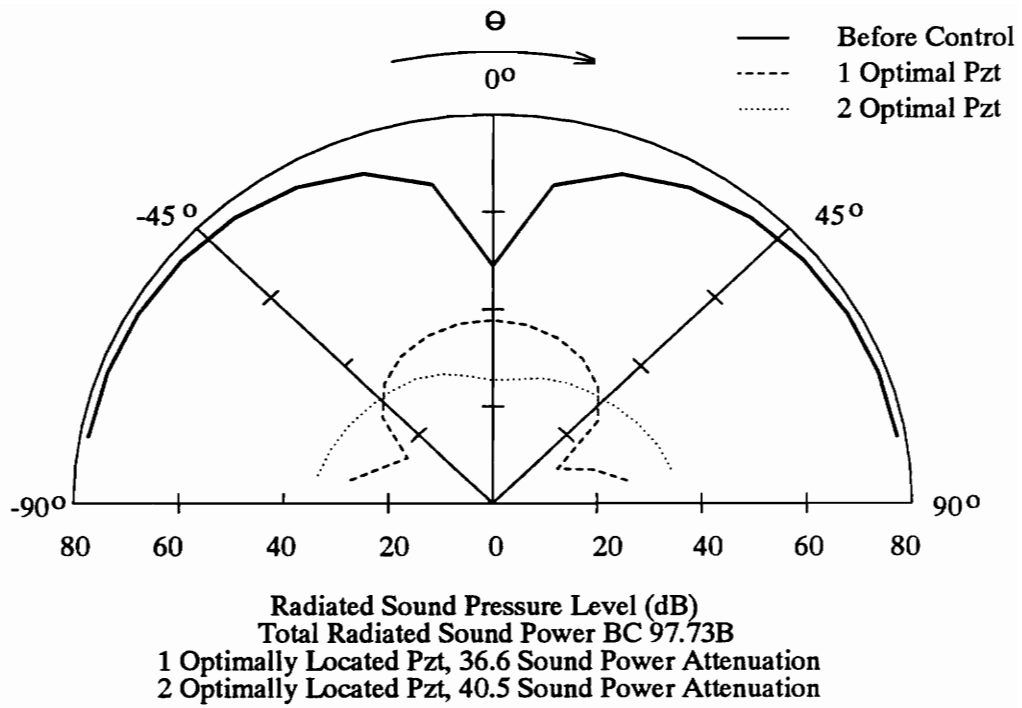


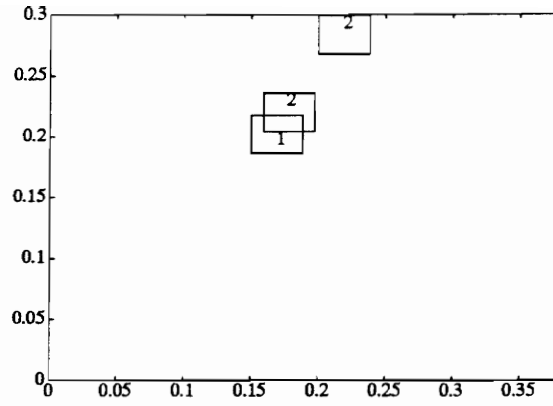
Figure 7.8: Directivity Pattern With 25% Center Mass

increases with mass. Therefore to achieve attenuation as mass increases, restructuring must be done away from this mode resulting in a directivity pattern becoming less dominated by mode four and more dominated by mode one. The directivity pattern using two channel control is relatively smooth with a similar shape in the fifteen and twenty percent mass cases, and resembles the shape of the pattern before control in the twenty-five percent mass case. This implies modal restructuring, probably into mode three, and modal suppression, until the mass reaches twenty-five percent. The twenty-five percent mass case seem to be primarily controlled by modal suppression.

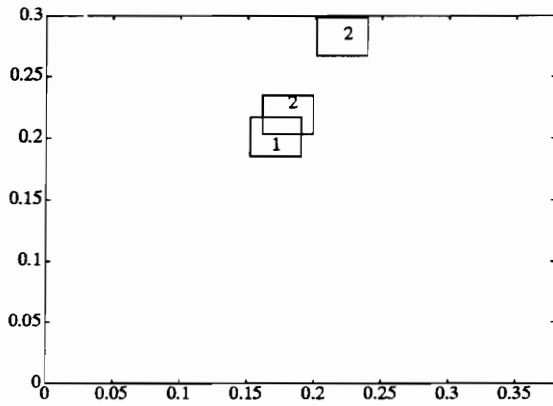
The single and multiple actuator pair locations are shown in Figure 7.9 for the various point mass models. The single actuator location shifted only slightly as the mass increased. When using two actuators the location of one did not stray far from the optimal location for a single actuator. The locations of the second actuator are very similar, differing most in the twenty-five percent mass case.

The plots of the objective function used to optimize the single actuator location for the fifteen, and the twenty-five percent point masses are shown in Figure 7.10, and Figure 7.11. It can be seen from these plots that the magnitude of the objective function increases by roughly an order of magnitude with the increase in the point mass. The plot of the objective function used to locate the target values for the two

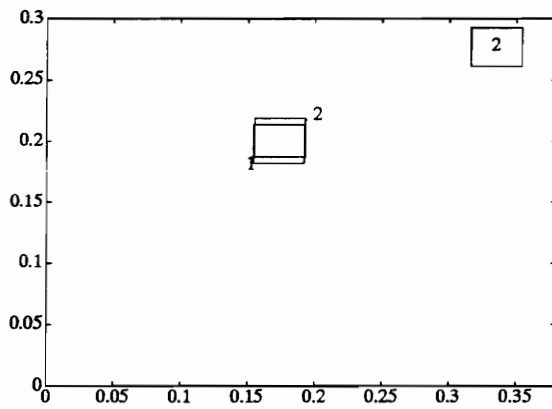
channel control case with the fifteen percent mass is shown in Figure 7.12. Using two actuators, the range of the objective function decreased by a factor of five with the increase in the point mass.



A: 15% Mass



B: 20% Mass



C: 25% Mass

Figure 7.9: Control Actuator Locations With Center Mass

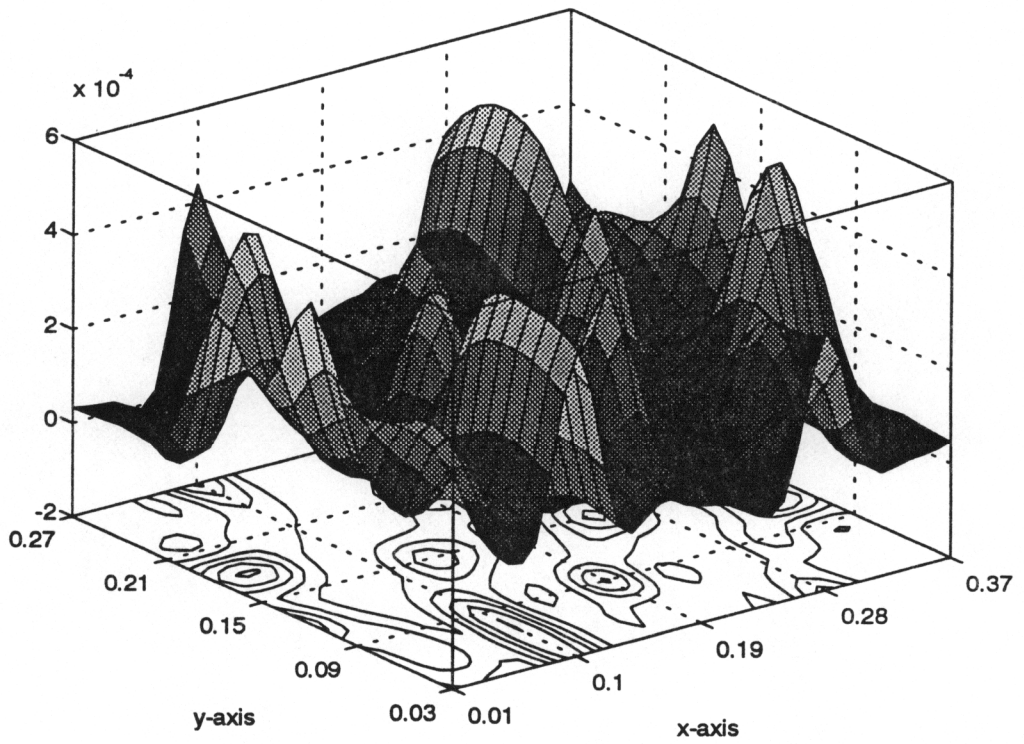


Figure 7.10: Objective Function For 1 PZT With 15% Center Mass

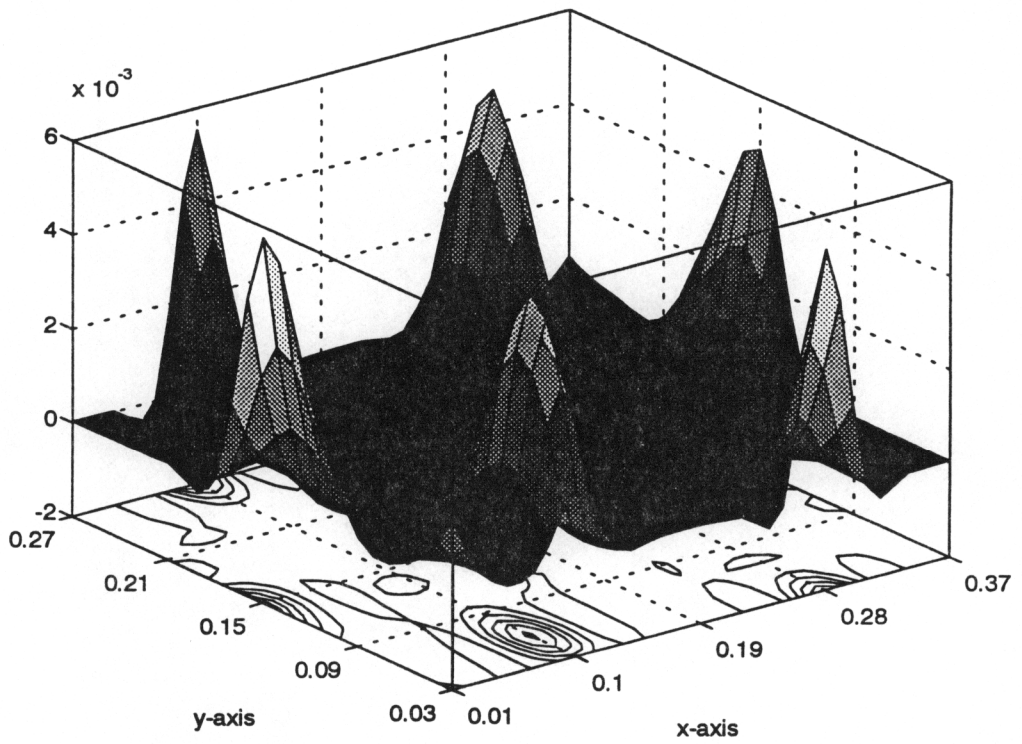


Figure 7.11: Objective Function For 1 PZT With 25% Center Mass

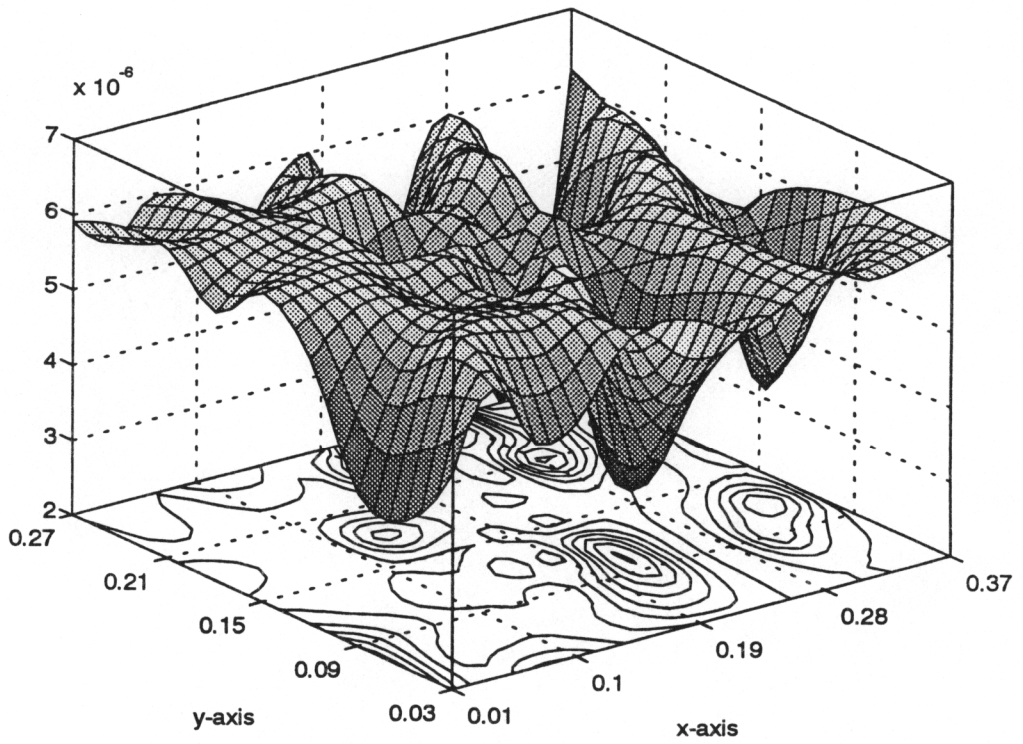


Figure 7.12: Objective Function For 2 PZTs With 15% Center Mass

7.3 Off Center Point Mass

This section will use the numerical model to study the results of placing a point mass at the coordinates (.14, .176). This location is diagonally symmetric to the location of the primary point force excitation. The location of the primary source was calculated to avoid the node lines of the first twenty-five theoretical mode shapes. Like the previous section, point mass elements were used which correspond to ten, fifteen, twenty, and twenty-five percent of the plate mass. Again the primary off resonance excitation is a 550 Hz pure tone point force.

The modal indices and natural frequencies are presented in Table 7.5. Although many of the natural frequencies do not change with increasing mass, the natural frequencies that do change decrease with increasing mass. It seems curious at first that the frequencies for mode five, seven, nine, and eleven do not change. Looking at the mode shapes shown in Figure 7.13, it can be seen that the added mass changes the mode shapes just enough that the mass element is on a node line as indicated by the circle. The node lines of mode five are on longer horizontal, but have rotated clockwise more than ten degrees. These mode shapes have node lines that are not as well defined as those for the plate without the point mass. Mode nine has a "dead spot," or place with very little displacement, in the center causing the mode to try to form its shape closer to the edges of the plate.

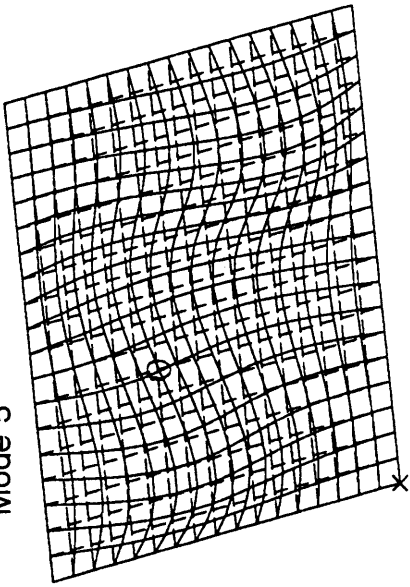
These mode shapes only change slightly, unlike the mode shapes of mode four, six, eight, and ten which have basically become unrecognizable as shown in Figure 7.14. Modes six and eight are almost mirror images of each other in the X direction except for some discrepancy along the bottom edge of the plate.

Table 7.5: Natural Frequencies With Off Center Mass

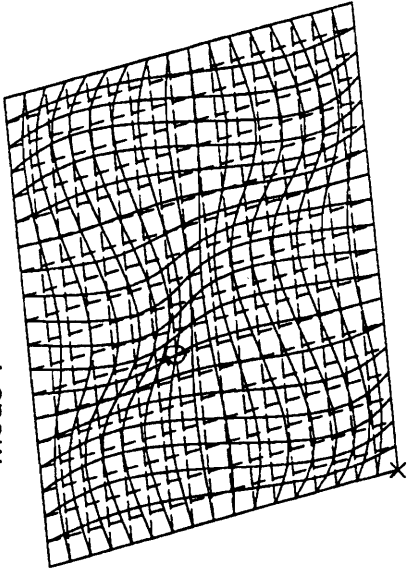
Mode	X Index	Y Index	10% Mass	15% Mass	20% Mass	25% Mass
1	1	1	75	70	66	63
2	2	1	171	166	163	161
3	1	2	238	236	235	233
4*	2	2	331	327	324	322
5	3	1	348	348	348	348
6*	1	3	457	442	433	427
7	3	2	505	504	504	504
8*	4	1	542	539	537	536
9	2	3	603	602	602	602
10*	4	2	712	708	705	704
11	3	3	759	759	759	759

The radiation efficiency of each mode with the various point masses is tabulated in Table 7.6. From this data it can be seen that the efficiency is relatively constant

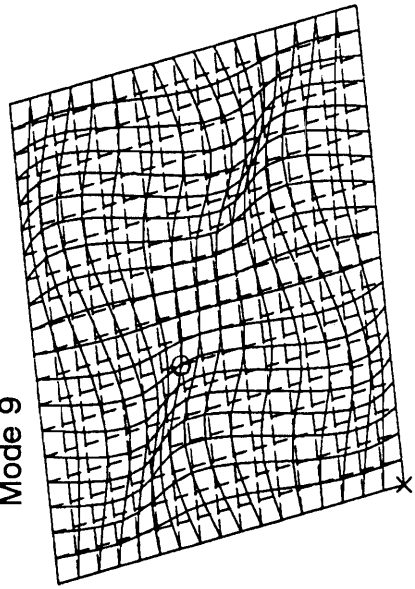
Mode 5



Mode 7



Mode 9



Mode 11

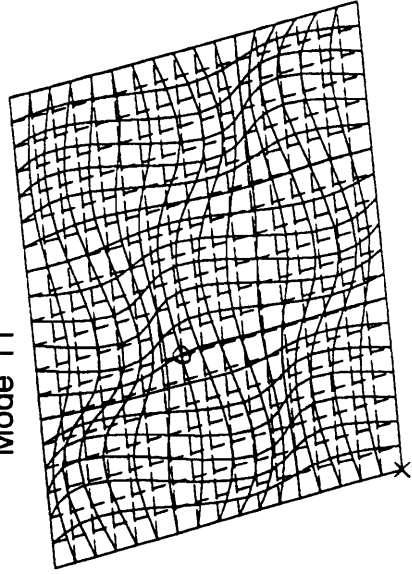
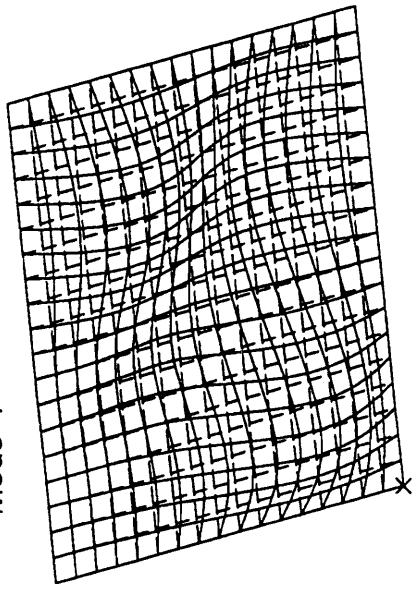
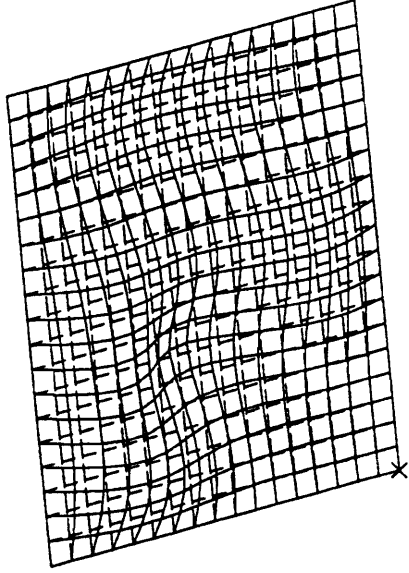


Figure 7.13: Slightly Deformed Modes Shapes With Off Center Mass

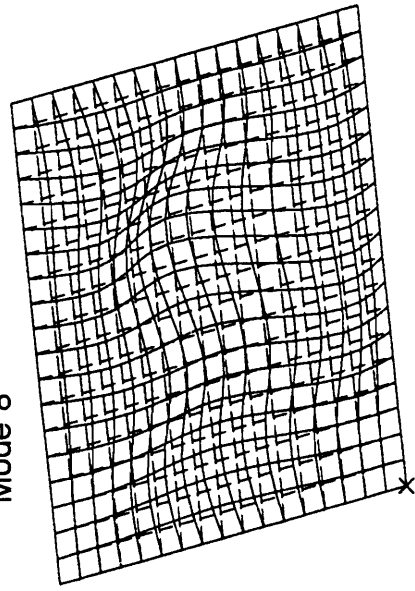
Mode 4



Mode 6



Mode 8



Mode 10

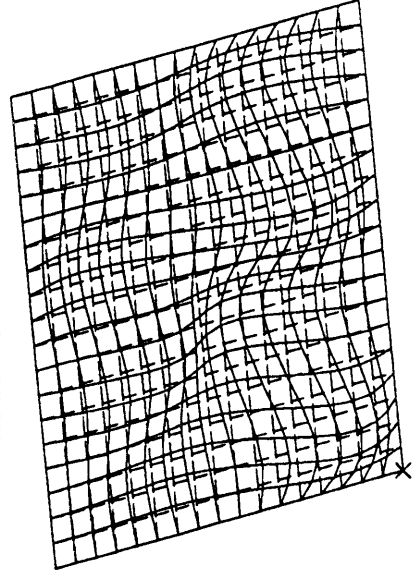


Figure 7.14: Majorly Deformed Mode Shapes With Center Mass

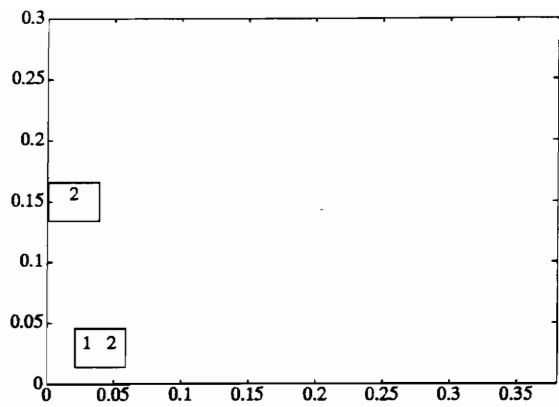
Table 7.6: Radiation Efficiency With Off Center Mass

Mode	10% Mass	15% Mass	20% Mass	25% Mass
1	.839	.837	.834	.832
2	.300	.336	.369	.398
3	.188	.198	.206	.213
4	8.444E-2	.117	.143	.163
5	6.095E-2	6.115E-2	6.108E-2	6.097E-2
6	.197	.217	.221	.219
7	1.598E-2	1.545E-2	1.523E-2	1.511E-2
8	5.110E-2	4.728E-2	4.554E-2	4.459E-2
9	4.167E-3	3.794E-3	3.613E-3	3.507E-3
10	1.569E-2	1.803E-2	1.938E-2	2.024E-2
11	2.504E-3	2.604E-2	2.678E-3	2.732E-3

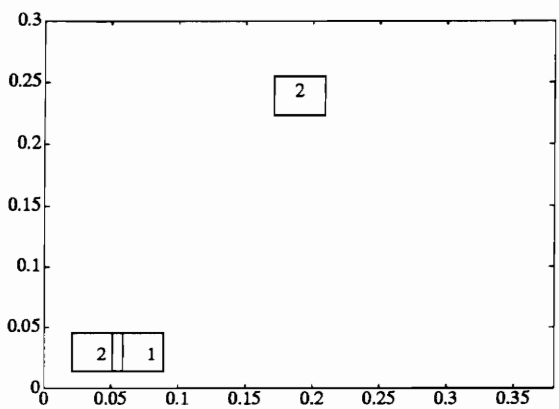
as the point mass increases, with the exception of mode four and mode eleven. For mode four the upper left quadrant of the plate is relatively flat due to the mass, and therefore has a greater net displacement making it a better radiator. When the mass is decreased this does not occur and the mode shape looks more like the typical (2,2) mode which is a relatively poor sound radiator. In the two previous sections the radiation efficiency dropped off severely after mode three for the simple structure and after mode four for the centered point masses. The radiation efficiency for this case drops off severely at mode five. This is because of the node

line rotation discussed above, which creates "dead spots in the upper right and lower left corners, causing the mode shape to have less averaged displacement. The efficiency of mode six is higher than that of mode three and then the efficiency drops off again for modes above six. As was stated earlier modes six and eight were said to be similar except for the section along the bottom of the plate. This difference in shape causes mode six to be a much better radiator due to the net displacement of the mode shape.

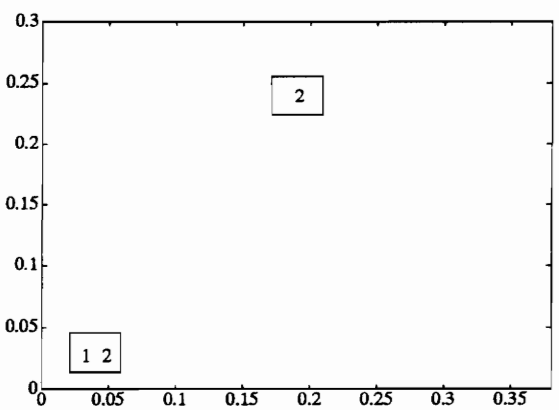
The directivity patterns for the controlled plate with off center point masses of fifteen, twenty, and twenty-five percent of the plate mass are shown in Figure 7.15, Figure 7.16, and Figure 7.17, respectively. The radiated sound power before control and the sound power attenuation after control for each mass case is tabulated in Table 7.7. The Control Actuator Locations are shown in Figure 7.18. From this data it can be seen that the sound power before control decreases slightly as mass increases. This is probably due to the fact that the frequency of mode eight, the closest mode shape to the primary disturbance, drops five Hz further away from the frequency of the primary disturbance and is therefore not as close to being at resonance. The radiation efficiency of this mode does decrease slightly with increasing mass but is of little significance as compared to some of the lower order modes.



A: 15% Mass



B: 20% Mass



C: 25% Mass

Figure 7.18: Control Actuator Locations With Off Center Mass

Table 7.7: Sound Power And Attenuation With Off Center Mass

Off Center Point Mass	Before Control Sound Power (dB)	Sound Power Attenuation 1 Pzt (dB)	Sound Power Attenuation 2 Pzts (dB)
15% Mass	87.2	17.8	22.6
20% Mass	85.8	16.3	21.3
25% Mass	85.0	16.2	20.6

It was also noticed that although the efficiencies for mode two were slightly higher than those of the centered mass case there is no notch in the directivity pattern before control. This is possibly due to the significant contribution of mode six to the off center point mass models. It is also noticed that mode four, the (3,1) mode shape for the centered mass, contributed much more to the radiation than it does in the off center mass case, mode five; whereas, mode four, the (2,2) mode shape for the off center mass, has a much higher efficiency than it does in the centered mass case, mode four. It should also be kept in mind that not only are there more mode shapes that are distorted in the off center point mass models than in the centered mass models, but these mode shapes are also distorted more severely.

The directivity patterns with one control actuator are similar in shape. As the point mass increases the area around the notch changes and another notch begins forming around thirty degrees. From the optimal actuator locations shown in Figure 7.18 it can be seen that for the single actuator case the actuator shifts slightly in the positive X direction for the twenty percent point mass case.

When two control actuators are used the directivity patterns for the various masses are similar except for the severity of the notches. It can be seen from Figure 7.18 that the actuator location of the second actuator changes between the fifteen, and the twenty percent mass case and is retained for the twenty-five percent mass case. It is also interesting that although the twenty percent mass case strayed slightly for the single optimal actuator location, the location of one actuator using multiple control is the same for each off center point mass. The location of the second actuator changes as the mass exceeds twenty percent of the plate mass.

In order to show how close some of these location solutions are Figure 7.19 shown the directivity pattern for the twenty-five percent mass case using the actuator locations for the fifteen percent mass case. The double actuator pair directivity patterns are different from Figure 7.17, however the total attenuation only differs by .1 dB.

As shown in Table 7.7 the attenuation achievable for the single and multiple actuator case decreases with increasing mass, but is relatively constant when taking into account the change in sound power before control. The addition of the second actuator increases the amount of attenuation by roughly 5 dB. The objective function used to optimize the single actuator location for the twenty percent mass case is shown in Figure 7.20. The objective function used to target the second actuator location for the twenty percent mass case is shown in Figure 7.21. The objective function plots for the fifteen and twenty-five percent mass cases for both single and multiple actuator cases are almost identical to the twenty percent mass case and are therefore not shown.

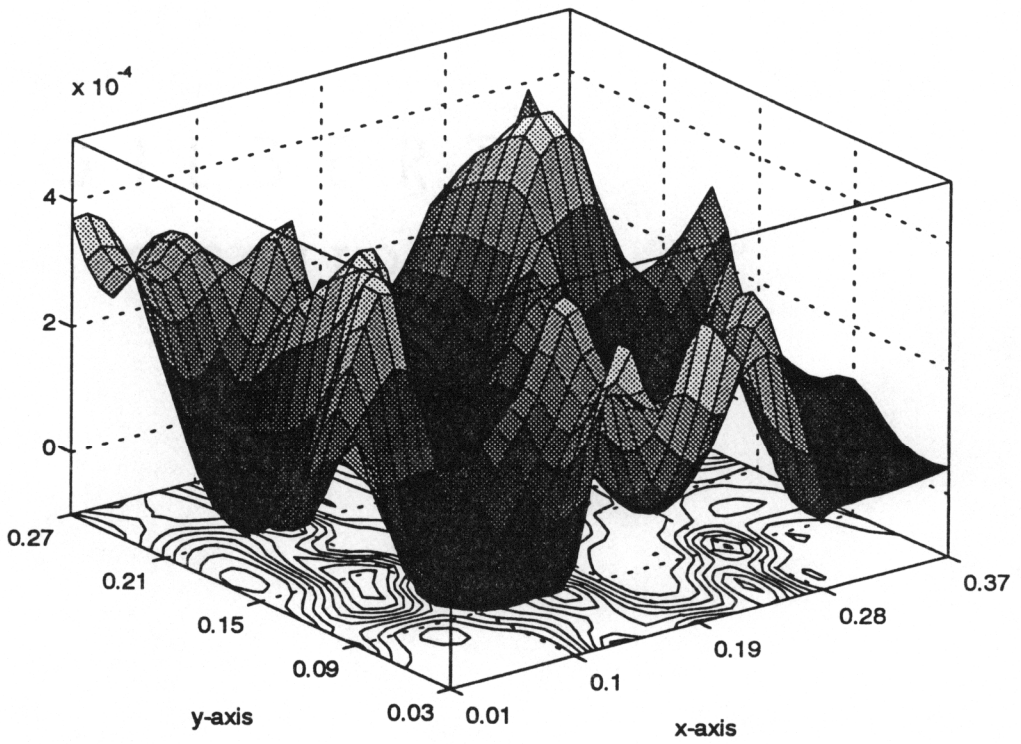


Figure 7.20: Objective Function For 1 PZT With 20% Off Center Mass

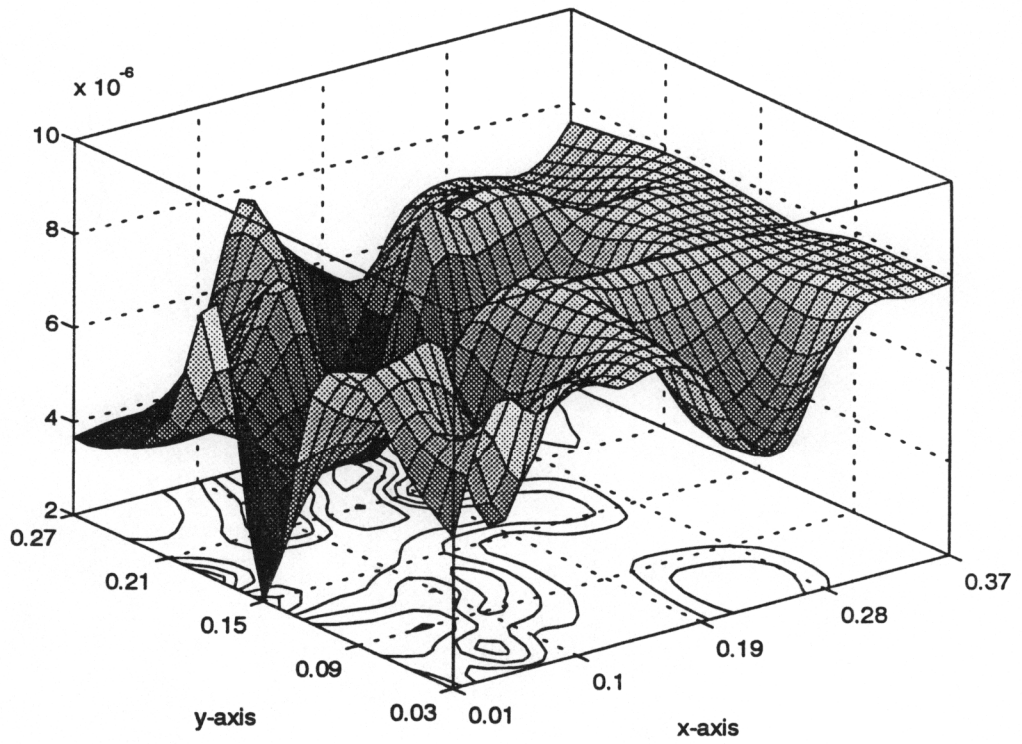


Figure 7.21: Objective Function For 2 PZTs With 20% Off Center Mass

Chapter 8

Line Mass Parametric Study

This section will use the numerical model to discuss the effects of adding a line mass to the simply supported flat plate. The plate is modelled with nineteen elements in the X direction. A line mass was placed vertically on the third element in the X direction. This location was chosen to avoid node lines of the structure at the driven frequency. This location would be near the node line of mode (6,1), which is beyond the decided range of significantly contributing modes.

The masses used in this study correspond to fifteen, twenty-five, fifty, and one hundred percent of the mass of the plate. The natural frequencies are tabulated in Table 8.1, and their corresponding 'modal indices' are shown in Table 8.2. From this data it can be seen that the natural frequencies decrease with increasing mass. It is also obvious that the line mass is not on a node line of the new 'deformed' mode shapes.

Most every homogeneous mode shape was distorted to some degree by the line mass as compared to the mode shapes of the plate with no line mass. The vertical node lines of the odd-odd and odd-even modes are shifted to the left. The first

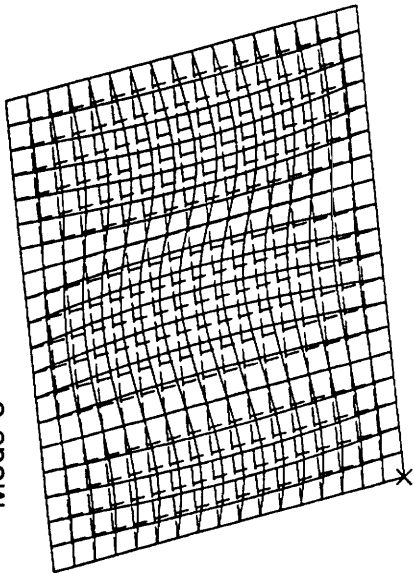
node line moves the most and the others space themselves out fairly evenly, as can be seen in Figure 8.1. The mode shapes with no vertical node lines have greater amplitude on the left side of the plate and flatten out towards the right as in mode seven also shown in Figure 8.1.

Table 8.1: Natural Frequencies With Line Mass

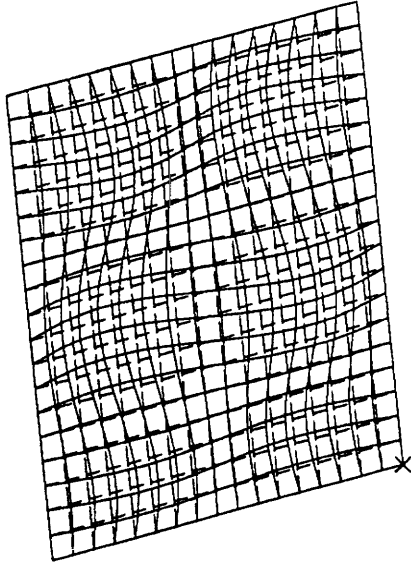
Mode	15% Mass	25% Mass	50% Mass	100% Mass
1	84	52	78	71
2	171	163	148	133
2	237	230	207	169
4	314	299	281	270
5	317	304	287	273
6	458	443	372	289
7	485	449	425	414
8	541	527	510	435
9	556	542	533	495
10	680	666	570	530
11	700	685	649	612

Table 8.2 shows that for the various line mass cases the mode shapes of the plate are the same for the first four modes, and then begin to change in their order as

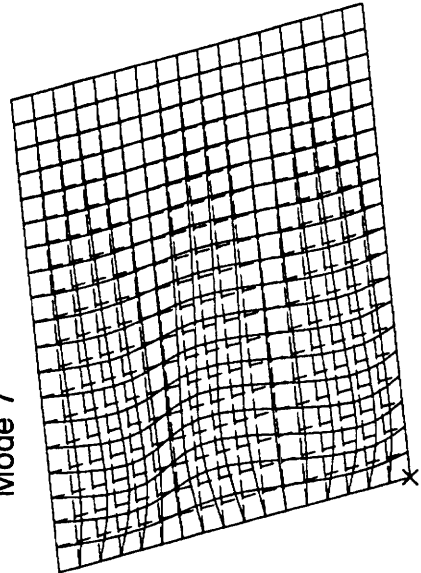
Mode 5



Mode 6



Mode 7



Mode 9

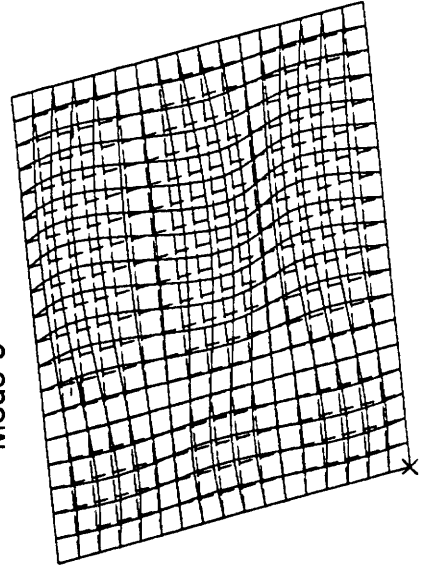


Figure 8.1: Deformed Mode Shapes With Line Mass

the mass increases. For example modes six and seven change order after the mass exceeds twenty-five percent of the plate mass. The mode shapes are the same for the fifteen and twenty-five percent line mass cases. The mode shapes of the fifty percent mass case also agree up to mode ten, except for the reversal of mode six and seven. At mode ten of the fifty percent line mass case a new mode shape, the (1,4) mode shows up, which appears as mode eight in the one hundred percent mass case.

The radiation efficiency of each of these modes is tabulated in Table 8.3. From this table it can be seen that the radiation efficiency of mode two increases significantly with increasing mass. The radiation efficiencies for the fifteen, twenty-five, and fifty percent line mass case drop off significantly after mode three. It can be seen that as mass increases the degree of this drop off becomes less significant. In fact the radiation efficiency for the one hundred percent line mass case does not drop off significantly until after mode five. This is because as the mass increases the mode shapes become more deformed in such a way as to have more net displacement resulting in a more efficient radiating mode.

The before and after control directivity patterns for the fifteen, twenty-five, fifty, and one hundred percent line mass case are shown in Figure 8.2, Figure 8.3, Figure 8.4, and Figure 8.5. The directivity pattern for the fifteen percent line mass

Table 8.2: Modal Indices With Center Line Mass

Mode	15% Mass (X Y) Modal Index	25% Mass (X Y) Modal Index	50% Mass (X Y) Modal Index	100% Mass (X Y) Modal Index
1	1 1	1 1	1 1	1 1
2	2 1	2 1	2 1	2 1
3	1 2	1 2	1 2	1 2
4	2 2	2 2	2 2	2 2
5	3 1	3 1	3 1	3 1
6	3 2	3 2	1 3	1 3
7	1 3	1 3	3 2	3 2
8	4 1	4 1	4 1	1 4
9	2 3	2 3	2 3	4 1
10	4 2	4 2	1 4	2 3
11	3 3	3 3	4 2	1 5

has a flat section in the quadrant between zero and forty-five degrees, due to the low radiation efficiencies of modes two, four, and five. The before control directivity pattern for the twenty-five percent line mass case regains a smooth curvature while the patterns for the fifty and one hundred percent line mass case have a decreasing radius of curvature proceeding from zero to ninety and negative ninety degrees.

Table 8.3: Radiation Efficiency With Line Mass

Mode	15% Mass	25% Mass	50% Mass	100% Mass
1	.847	.848	.849	.847
2	.270	.284	.345	.481
3	.174	.173	.161	.143
4	3.809E-2	5.288E-2	9.726E-2	.128
5	3.522E-2	4.460E-2	7.532E-2	.110
6	6.637E-2	7.755E-3	3.766E-2	3.412E-2
7	5.153E-2	4.514E-2	1.166E-2	1.502E-2
8	2.905E-2	3.095E-2	3.646E-2	1.535E-2
9	2.938E-2	3.872E-2	4.528E-2	4.055E-2
10	5.865E-3	7.033E-3	1.646E-2	4.745E-2
11	5.120E-3	7.670E-3	8.669E-3	7.870E-3

The after control directivity patterns for the fifteen percent mass model for both one and two actuator pairs are almost identical. It can also be seen that only .3 dB of attenuation is gained by adding a second actuator pair. Following the directivity pattern for one actuator pair through the increasing line mass, it can be seen that the deep notches just above forty-five and negative forty-five degrees in the fifteen percent mass case, smooth out as mass increases and then reform just below forty-five and negative forty-five in the one hundred percent line mass case. The directivity patterns for the two actuator control case retain their notches through the fifty percent line mass case but become smooth in the one hundred percent line

mass case.

The before control radiated sound power along with the amount of attenuation with one and two pairs of actuators is shown in Table 8.4. From this data it is shown that the twenty-five percent line mass case had the highest radiated sound power before control, and likewise the greatest amount of attenuation. The sound power attenuation for the other three line mass cases only differ by about five dB. When observing this data one should take note of the natural frequencies of the various line mass cases.

Table 8.4: Sound Power And Attenuation With Line Mass

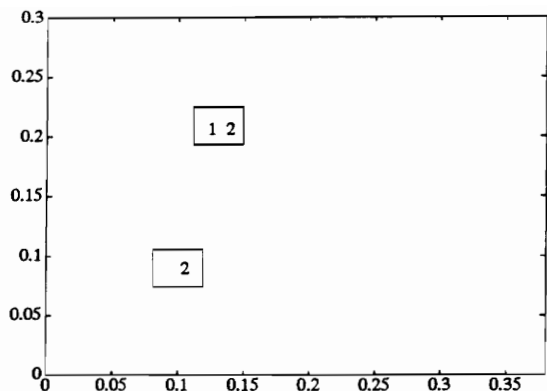
Line Mass	Before Control Sound Power (dB)	Sound Power Attenuation 1 Pzt (dB)	Sound Power Attenuation 2 Pzts (dB)
15% Mass	81.69	18.1	18.4
25% Mass	88.45	25.7	27
50% Mass	82.06	21.1	22.9
100% Mass	79.46	16.3	19.4

The driving frequency for this study is 550 Hz, off resonance excitation. The closest natural frequency to this primary disturbance is mode nine of the fifteen

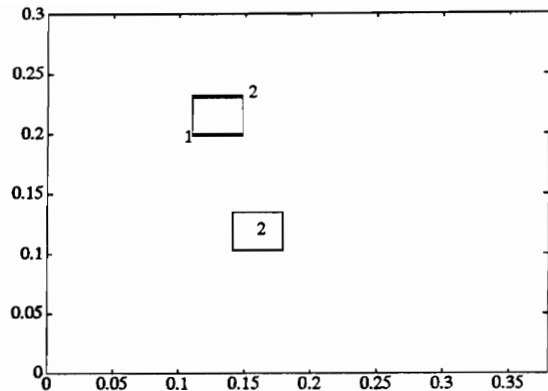
percent line mass case followed by mode nine of the twenty-five percent line mass case. For this reason one might expect the fifteen percent line mass case to have the highest radiated sound power. The primary disturbance is on opposite sides of the resonances of these two line mass cases, thus coupling different modes. In other words, most of the energy put into the structure by the disturbance goes into the modes that are closest in frequency to the disturbance. Because these closest modes are different for the various line mass cases, different modes have the most significant coupling into the response. The natural frequency for mode eight of the fifteen percent line mass case is also very close to the primary disturbance frequency. This causes a 'battle' for dominance between the two mode shapes. Structures at resonance or close to resonance have a greater response to the excitation because most of the disturbance energy is going into one mode. However, if there is a mode close to both sides of the disturbance frequency the disturbance energy is distributed mostly to those two modes, and the response is generally less.

The amount of attenuation with one actuator increases with the increase in radiated sound power before control. It is also noticed that the amount of additional attenuation gained by the second actuator pair increased with increasing mass. However, very little extra attenuation was achieved by adding the second actuator pair, about 3 dB at most.

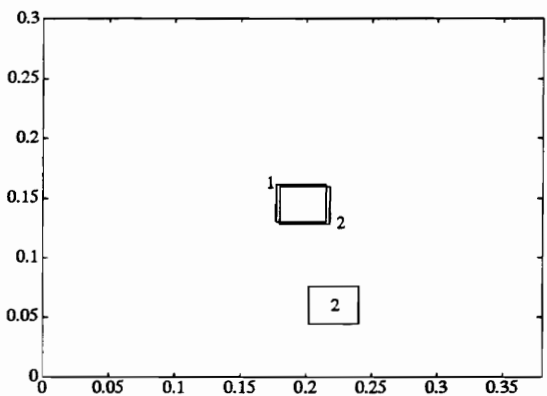
The optimal actuator locations for the various line mass cases are shown in Figure 8.6. From this data it can be seen that the optimized location for the single actuator is in the same general area, with the Y coordinate increasing slightly with mass, with the exception of the twenty-five percent line mass case. Upon adding the second actuator the location of the single actuator is retained except in the one hundred percent line mass case in which the X coordinate moves toward the edge of the plate. The location of the second actuator pair is the same for the one hundred and the fifteen percent line mass case, but is very different for the remaining line mass cases. This is because as the line mass increases the plate begins to respond as if it were two separate plates. The objective functions for locating the optimal single and double actuator pair for the fifty percent line mass case are shown in Figure 8.7 and Figure 8.8.



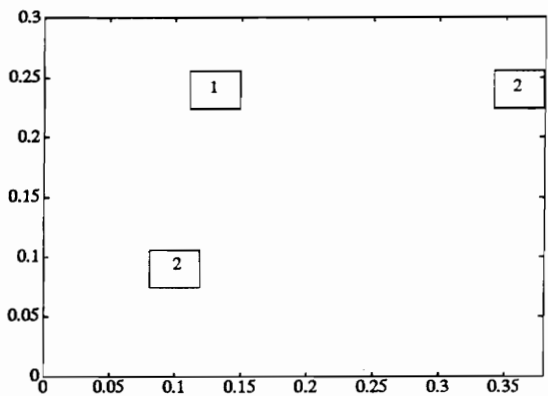
A: 15% Mass



B: 25% Mass



C: 50% Mass



D: 100% Mass

Figure 8.6: Control Actuator Locations With Line Mass

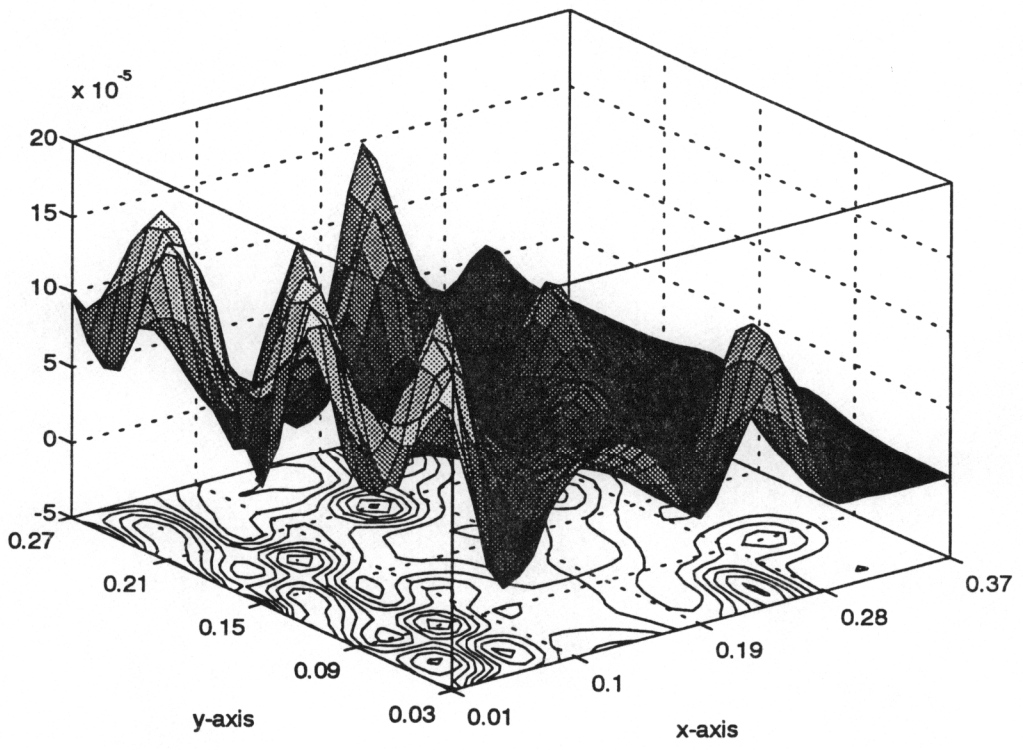


Figure 8.7: Objective Function For 1 PZT With 50 % Line Mass

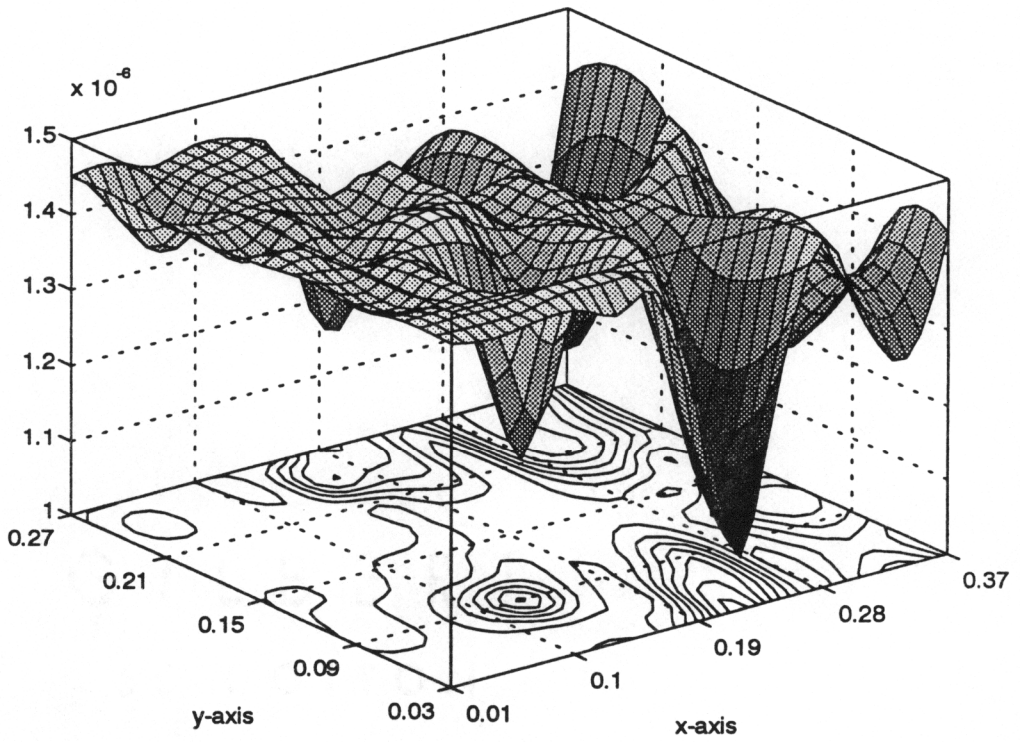


Figure 8.8: Objective Function For 2 PZTs With 50 % Line Mass

Chapter 9

Spring Mass Parametric Study

This section will use the numerical model to investigate the effect of adding a spring mass system to the surface of the simply supported plate. The location of the spring mass system was chosen to correspond with the location of the off center point mass used in Chapter 7 in order to avoid node lines. To develop this model an additional node, node 361, was placed 1 centimeter above node 208 at coordinates (.14, .17647). A node to node translational spring element was then added to the structure. The spring element was defined to be uni-axial, allowing translation in the Z direction only. Likewise, the degrees of freedom for node 361 were restrained from motion except in the Z direction. A mass element of .0172 kg was then added to node 361.

A relatively light mass was chosen so the effect of the single degree of freedom system would not dominate the response of the entire system, which is the plate with the spring mass system attached to its surface. In order to "tune" the resonance of the spring mass system to that of the excitation frequency the mass was required to be small. The natural frequency of a spring mass system is governed by the following equation:

$$\omega_n = \sqrt{\left(\frac{k}{m}\right)} \quad (9.1)$$

where k is the translational spring stiffness in (N/m), and m is the point mass in kg. This spring mass system is mounted to the plate so the above equation becomes an approximation to the resonant frequencies which will change due to the plate dynamics. The plate response will change also due to the coupling with the spring mass system. The natural frequencies of the new system, the plate with the attached spring mass should decrease slightly due to the increase in mass. The primary disturbance is again a 550 Hz point force excitation. The spring mass system was designed to be at resonance at 550 Hz. In order to achieve this design parameter the mass had to be small in order to avoid having a spring that was approaching infinite stiffness. The spring constant for this design was 2.05E+05 N/m. Two other design cases will be shown in which the spring constant was varied by a factor of two in order to allow the spring mass system to be excited above and below resonance. These spring constants were 1.025E+05 and 4.1E+05 corresponding to resonance frequencies of 389 and 777 Hz respectively. It should be noted that these frequencies are not close to resonant frequencies of the plate.

The natural frequencies for the structure containing a spring mass system which is excited below resonance, at resonance, and above resonance are shown in Table 9.1. From this data it can be seen that the natural frequencies are constant with increasing spring stiffness until mode six. For modes above six the natural frequency increases with increasing spring stiffness. These natural frequencies for the below resonance spring mass case are consistent and slightly lower than those of the homogeneous plate with exception of the addition of mode six for the spring mass system plate.

Table 9.1: Natural Frequencies With Spring Mass System

Mode	Below Resonance	At Resonance	Above Resonance
1	84	84	84
2	182	183	183
3	243	244	244
4	337	340	340
5	349	350	350
6	392	485	502
7	504	505	507
8	518	537	565
9	594	601	603
10	609	634	716
11	736	740	759

The modal indices for these modes are listed in Table 9.2. Many of these mode shapes are deformed or distorted as compared to the mode shapes of the homogeneous plate. Mode six is distorted to the point of being unrecognizable for all three spring rates. As expected the model containing the on resonance spring mass system has more distorted mode shapes than the other cases. This is because the response of the spring mass system is greatest when at resonance and therefore has more of an effect on the vibration of the plate. Modes eight through ten are unrecognizable for the on resonance spring mass system, but only slightly distorted for the other two spring rates. For the above resonance spring mass case mode shape seven appears to be the inverse of mode shape six.

The radiation efficiencies for these mode shapes are shown in Table 9.3. From this data it can be seen that the radiation efficiencies drop off significantly after mode three. For the below and at resonance cases, the radiation efficiency of mode six is close to that of mode four, and then drops off again. This is due to the net displacement of the mode shapes.

To get a perspective of the magnitude of the spring rates used, an effective stiffness was calculated for the plate. This effective stiffness was calculated by observing the maximum displacement of the plate with an applied unit force. The

Table 9.2: Modal Indices With Spring Mass System

Mode	Below Resonance (X Y) Index	At Resonance (X Y) Index	Above Resonance (X Y) Index
1	1 1	1 1	1 1
2	2 1	2 1	2 1
3	1 2	1 2	1 2
4	2 2	2 2	2 2
5	3 1	3 1	3 1
6	*	*	*
7	3 2	3 2	*
8	1 3	*	4 1
9	4 1	*	2 3
10	2 3	*	4 2
11	4 2	4 2	3 3

unit force divided by the displacement gives a relative stiffness of $4E+05$ N/m. Another check was performed to ensure that the spring was not approaching an infinite stiffness. The point mass was applied directly to the surface of the plate at the same location. The result of this test was that the natural frequencies above mode five increased significantly and the corresponding mode shapes showed very little if any distortion.

Table 9.3: Radiation Efficiencies With Spring Mass System

Mode	Below Resonance	At Resonance	Above Resonance
1	.844	.844	.845
2	.260	.260	.260
3	.173	.172	.172
4	4.501E-2	3.391E-2	3.291E-2
5	5.950E-2	5.432E-2	5.308E-2
6	.148	.125	3.625E-2
7	1.266E-2	1.702E-2	5.043E-2
8	4.586E-2	4.505E-2	6.630E-2
9	2.413E-2	1.731E-3	7.214E-3
10	3.449E-2	4.347E-2	1.330E-2
11	6.116E-3	6.077E-3	2.699E-3

The directivity patterns for the plate with below resonance, at resonance, and above resonance, spring mass systems are shown in Figure 9.1, Figure 9.2, and Figure 9.3. The total radiated sound power before control increases as the spring rate increases. As the spring rate increases the natural frequency of mode eight moves closer to the disturbance frequency of 550 Hz; however, mode eight is an entirely different shape for these various cases. The before control directivity pattern for the plate with the spring mass system tuned to be driven below its resonance is smooth and flat on top. A notch develops at zero degrees and gets

deeper as the spring stiffness increases. This is due mostly to mode eight which is the (1,3) mode shape for the below resonance case and the (4,1) mode shape for the above resonance case.

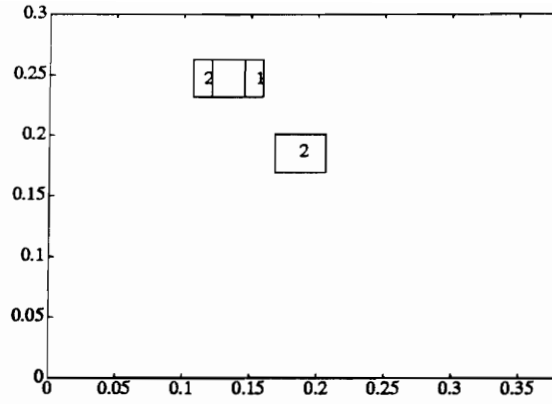
In accordance with the other studies, the amount of attenuation increases as the sound power before control increases with the spring stiffness. The sound power and attenuation are shown in Table 9.4. The amount of attenuation achieved with one actuator is relatively low for the plate with the softer spring. The additional attenuation achieved with the use of a second actuator is fairly high, ranging from about 4 to 10 dB.

Table 9.4: Sound Power and Attenuation With Spring Mass System

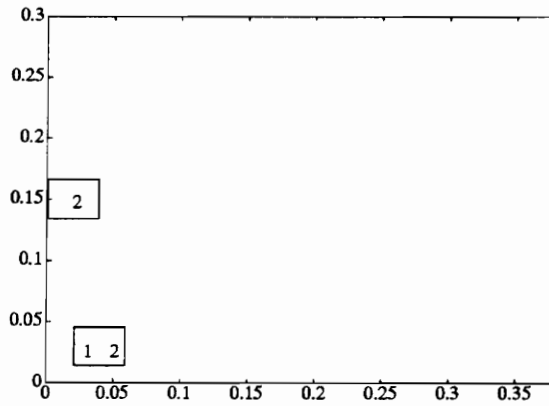
Resonance	Before Control Sound Power (dB)	Sound Power Attenuation 1 Pzt (dB)	Sound Power Attenuation 2 Pzts (dB)
Below	77.05	6.4	12.3
At	81.96	13.5	17.5
Above	87.62	15.9	25.5

It should be noted that the plate with the spring mass system at resonance should not be expected to have the most sound power. This at resonance system may have the most vibration energy; however, this does not imply that it has the most sound power. It should also be noted that the three models have spring mass systems that are tuned to different frequencies that are located between different natural modes of their corresponding structures.

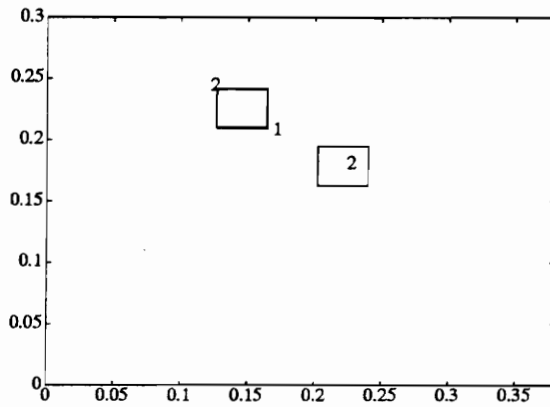
The locations of the actuators for the three systems are shown in Figure 9.4. Due to the differences in the systems the actuator locations were not expected to be as similar as in previous studies, especially in the at resonance case. The optimal locations for the single and double actuator pair in the below and above resonance cases are relatively close. The objective functions for finding the optimal single actuator locations show some of the same trends as can be seen by comparing Figure 9.5 with Figure 9.6. It can be seen that the optimal location for a single actuator did not move much when adding a second actuator in any of these cases. This was also expected using the logic that the control strategy would use one actuator to attack energy produced by the spring mass couple and the other to attack the remaining energy produced directly by the plate.



A: Below Resonance



B: At Resonance



C: Above Resonance

Figure 9.4: Control Actuator Locations With Spring Mass System

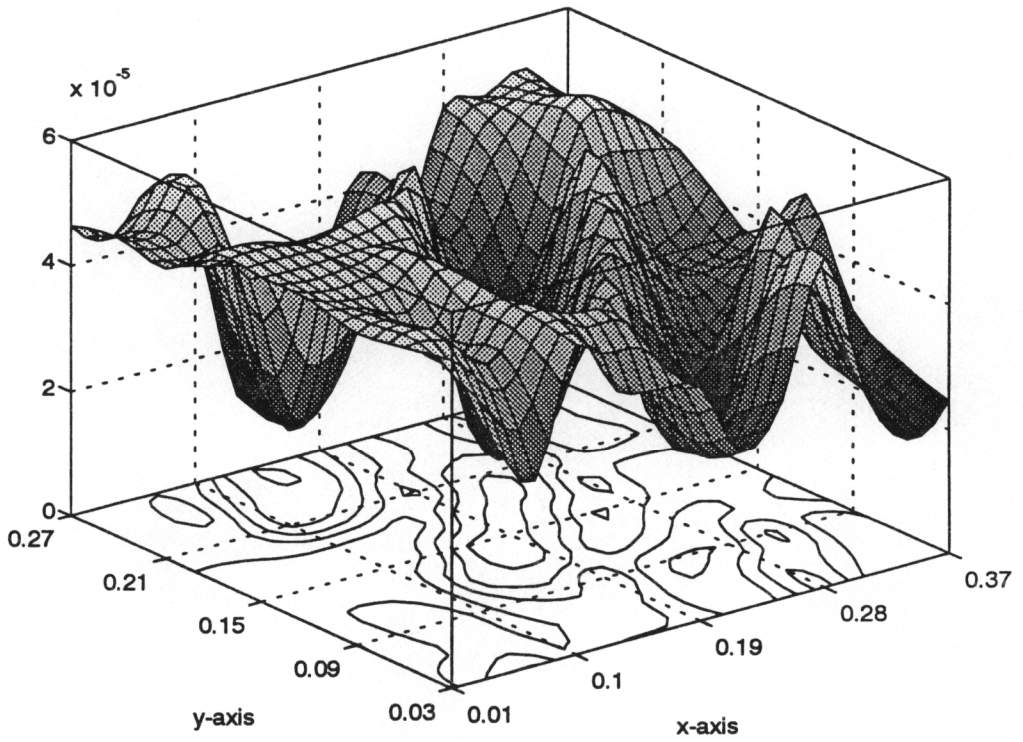


Figure 9.5: Objective Function For One PZT Below Resonance System

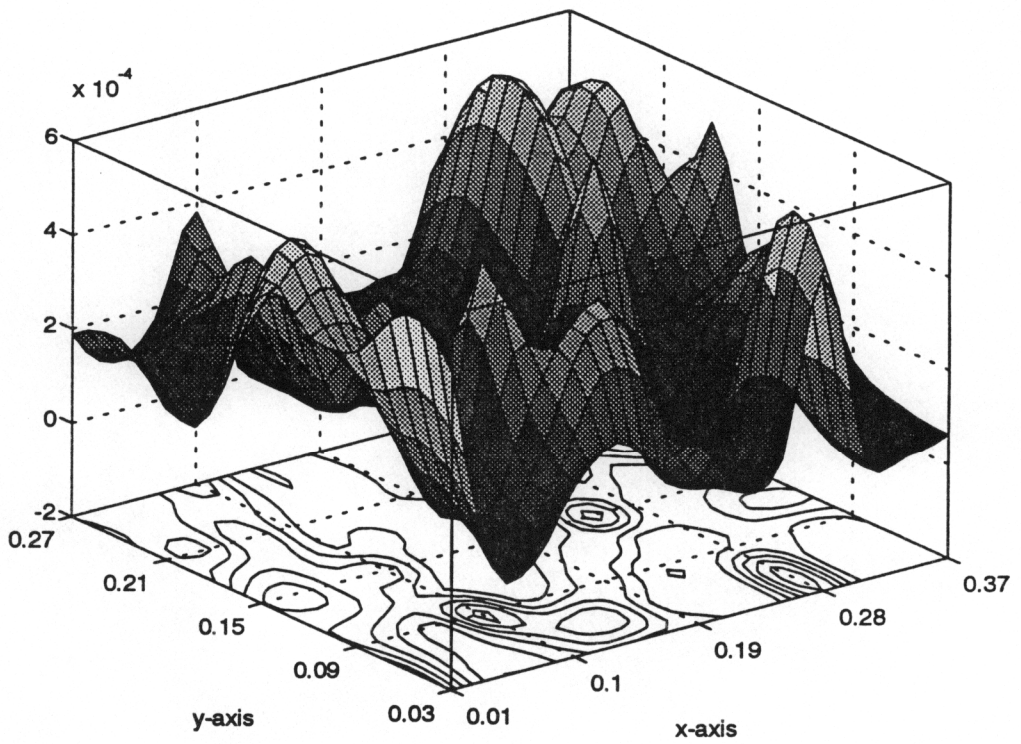


Figure 9.6: Objective Function For One PZT Above Resonance System

9.1 Multiple Actuators and Robustness

This system is the most complex system studied in this work and is believed to most closely resemble actual physical systems. For this reason some further aspects were considered. A third actuator was optimized in the below and above resonance cases. The additional sound power attenuation due to this third actuator was 1.6 and .5 dB respectively. Relative to the first two optimally located actuators, the third actuator provides almost no additional attenuation. This further confirms the previously noted concept of diminishing returns for additions of control actuators on structures with discontinuities.

Some robustness testing was also done on these spring mass systems. The first tests involve changing the optimal actuator location, while keeping the control forces and excitation frequency constant, to observe the decrease in attenuation. These tests were performed on the below and above resonance cases using one, two, and three actuators. In each case the actuator was first moved by half of its physical length, in the x, y, -x, and -y direction. The sound power at each of these locations was then averaged and could be compared to the sound power of the optimal actuator location. The test was then repeated moving a full actuator length in each of the four directions. These are substantial changes in location and the amount of attenuation that was lost ranged from 6 to 50 percent. In general the

further the actuators were moved from their optimal location the more attenuation was lost. From this data it can be determined that slight inaccuracies in physical placement of optimally located actuators on a structure will not significantly decrease the control achievable.

Another robustness test was done by keeping the control forces and locations constant and changing the excitation frequency. This test was done using the above resonance case. The frequency was varied in either direction by twenty hertz. This test was performed using one, two, and three actuators. The difference in achievable attenuation is negligible, at most 1 dB.

Chapter 10

Conclusions and Recommendations

A general procedure for the optimization of control actuator locations to minimize the total radiated sound power from complex structures has been developed. This optimization procedure interfaces finite and boundary element models with non-linear optimization techniques. The optimization procedure was used to perform parametric studies of Active Structural Acoustic Control (ASAC) for a simply supported plate with various discontinuities such as point mass, line mass, and spring mass systems. The system models were harmonically excited by an off resonance point force of 550 Hz and controlled by piezoceramic actuators. Although the excitation frequency is the same for each of the cases studied, the eigenproperties change with alteration of the physical parameters of the system. Therefore the excitation frequency for each case is effectively different, as is its response.

The accuracy of this sophisticated model was verified by comparing solutions from modal based analytical and assumed modes models for simple and complex structures. Some unique aspects of this procedure are that it requires a single implementation of the finite and boundary element solution, and that the finite

element forced response solution is not required. Therefore, this ASAC actuator optimization procedure shows potential for application to any structure that can be accurately modeled with finite element software. More complicated modeling aspects such as fluid coupling could be readily attacked.

This optimization procedure was very effective in reducing the total radiated sound power from these complex structures. The addition of optimized actuators resulted in additional attenuation of varying extent, highly dependent on the discontinuity. The locations of the optimized actuators were also found to be very sensitive to the discontinuity. Even small perturbations in the discontinuity can cause significant changes in the optimized actuator locations. This implies that unmodeled dynamics in the system could compromise the effectiveness of the optimized system performance. The systems responded well to slight changes in disturbance frequency, but attenuation was greatly compromised with slight changes in actuator location. In both of these robustness tests the control forces were held constant. It can therefore be determined that the control forces are more sensitive to changes in actuator location than disturbance frequency. This further emphasizes the need for actuator location optimization. It was also observed that in general the addition of the second and third actuator did not significantly change the position of the single optimal actuator location. As expected it was also found that as the systems approached resonance the sound power before control increased as did

the amount of attenuation achievable with a single optimized actuator. Under these circumstances it was also found that the addition of optimized actuators resulted in significantly less additional attenuation as compared to the single optimally located actuator.

The analysis of the data from the parametric study proved to be difficult due to the inherent definition of the study. For example, changing a single parameter such as the mass of a discontinuity caused many changes in the structural properties such as the shapes and order of the natural modes, and their corresponding natural frequencies. Possible improvements include a more detailed study where the parametric perturbations are small enough that the mode shapes do not change in order, and by varying the primary disturbance such that it is equidistant from the new natural frequencies of the various cases.

Further improvements in the modeling procedure could be realized in better interfacing of the various modeling software. The proper computer system, such as the RISC6000, with the ability to run the finite and boundary element analysis in SYSNOISE, and the FORTRAN optimization code, could also speed up this data transfer time and provide the means of developing a streamlined code to perform the entire optimization procedure.

Bibliography

- [1] B. Friedland, *Control System Design*, McGraw Hill, New York, New York, 1986.
- [2] C.E. Wilson, *Noise Control*, Harper & Row, 10 East 53rd Street, New York, NY 10022, 1989.
- [3] C.R. Fuller, C.A. Rogers, H.H. Robertshaw, "Active Structural Acoustic Control With Smart Structures" *Fiber Optic Smart Structures and Skins II*, Edited by Eric Udd, SPIE Vol. 1170, pp. 338-358, 1989.
- [4] M.C. Junger, and D. Feit, *Sound, Structures, and Their Interaction*, Massachusetts Institute of Technology, Second Edition, 1986.
- [5] Lueg, "Process of Silencing Sound Oscillator," U.S. Patent No. 2,043,416, 1936.
- [6] S.J. Elliot, and P.A. Nelson, "The Active Control Of Sound," *Electronics & Communication Engineering Journal*, pp. 127-136, 1990.
- [7] C.R. Fuller, Apparatus and Method for Global Noise Reduction," U.S. Patent No. 4,715,599, 1987.
- [8] C.R. Fuller, "Active Control of Sound Transmission / Radiation from Elastic Plates by Vibration Inputs: I Analysis," *Journal of Sound and Vibration*, 136(1), pp. 1-15, 1989.

- [9] R.L. Clark, "Advanced Sensing Techniques for Active Structural Acoustic Control," Ph. D. Dissertation, Virginia Tech, 1992.
- [10] B. Jaffe, R.S. Ruth, and S. Marzullo, "Piezoelectric Properties of Lead Zirconate-Lead Titanate Solid-Solution Ceramics," *Journal of Applied Physics*, 25(6), pp.809-810, 1954.
- [11] H. Kawai, "The Piezoelectricity of Poly (vinylidene Fluoride)," *Journal of Applied Physics*, 8(7), pp.975-976, 1969.
- [12] C.R. Fuller, and J.D. Jones, "Influence of Sensor and Actuator Location on the Performance of Active Control Systems," 87-WA / NCA-9, presented at ASME Annual Meeting, Boston, MA, December 1987.
- [13] C.R. Fuller, R.J. Silcox, V.L. Metcalf, and D.E. Brown, "Experiments on Structural Control Of Sound Transmitted Through an Elastic Plate," *Proceeding of the American Control Conference*, pp.2079-2089, 1989.
- [14] E.K. Dimitriadis, C.R. Fuller, and C.R. Rogers, "Piezoelectric Actuators for Distributed Vibration Excitation of Thin Plates," *Journal of Vibration and Acoustics*, 118, pp.100-107, January 1991.
- [15] B.T. Wang, E.K Dimitriadis, and C.R. Fuller, "Active Control of Noise Transmission Through Rectangular Plates Using Multiple Piezoelectric or Point Force Actuators," *Journal of the Acoustic Society of America*," 90(5), pp. 3313-3320, November 1991.

- [16] R.L. Clark, and, C.R. Fuller, "Experiments on Active Control of Structurally Radiating Sound Using Multiple Piezoceramic Actuators," *Journal of the Acoustic Society of America*, 91(6), pp.3313-3320, 1991.
- [17] R.L. Clark, and C.R. Fuller, "Optimal Placement of Piezoelectric Actuators and Polyvinylidene Fluoride (PVDF) Error Sensors in Active Structural Acoustic Control Approaches (ASAC)," *Journal of the Acoustic Society of America*, 92(3), pp.1521-1533, September 1992.
- [18] B.T. Wang, R.A. Burdisso, and C.R. Fuller, "Optimal Placement of Piezoelectric Actuators for Active Control of Sound Radiation from Elastic Plates," *Proceedings of Noise-Con*, pp.267-275, July 1991.
- [19] T. Song, and C.R. Fuller, "Optimization of Actuator Location and Control Robustness Analysis for Active Structural Acoustic Control," *Journal of the Acoustic Society of America*, (to appear) 1992.
- [20] P. Wagstaff, "Optimization of Control Force Input Positions To Reduce Radiated Noise of Vibrating Structures," *Proceedings of Recent Advances in Active Control of Sound and Vibration, Second Conference*, pp. 941-954, 1993.
- [21] L. Meirovitch, *Analytical Methods in Vibrations*, Macmillan Publishing Co., New York, NY, 1967.
- [22] D.A. Bies, and C.H. Hanson, "*Engineering Noise Control*," UNWIN Hyman, London, 1988.

- [23] C.E. Wallace, "Radiation Resistance of a Rectangular Panel," *Journal of the Acoustic Society of America*, 5(3), pp.946-952, 1972.
- [24] B.T. Wang, E.K. Dimitriadis, and C.R. Fuller, "Active Control of Structurally Radiated Noise Using Multiple Piezoelectric Actuators," *AIAA Journal*, 29(11), pp. 1802-1809, 1991.
- [25] R.L. Clark, and G.P. Gibbs, "A Novel Approach to Feedforward Higher Harmonic Control," *Journal of the Acoustic Society of America*, (to appear), 1993.
- [26] R.D. Cook, D.S. Malkus, and M.E. Plesha, "*Concepts and Applications of Finite Element Analysis*," John Wiley & Sons, New York, 1989.
- [27] IBM, CAEDS, Integrated Finite Element Solver (IFES), Users Guide, Publication # SH52 0266 00, 1990.
- [28] C. Knight, "*The Finite Element Method In Mechanical Design*," Virginia Tech, Mechanical Engineering Department, 1989.
- [29] K. Schittkowski, *Calculus With Analytic Geometry*, Prindle, Weber & Schmidt, Boston, MA, 1983.
- [30] K.R. Fyfe, J.G. Coyotte, and P.A. Van Vooren, "Acoustic and Elasto-Acoustic Analysis Using Finite Element and Boundary Element Methods," *Journal of Sound and Vibratton*, pp. 16-22, December 1991.
- [31] Sysnoise, Theoretical Manual, Dennison National Company.
- [32] R.L. Clark, C.R. Fuller, and A.L. Wicks, "Characterization of Multiple

Piezoelectric Actuators for Structural Excitation," *Journal of the Acoustic Society of America*, 90(1), July 1991.

[33] H.C. Lester, and C.R. Fuller, Active control of Propeller Induced Noise Fields Inside a Flexible Cylinder," *AIAA Journal*, 28(8), pp.1374-1380, 1990.

[34] *Users Manual: IMSL Math/Library*, 1989.

[35] R.L. Clark, and C.R. Fuller,"Modal Sensing of Efficient Acoustic Radiation with PVDF distributed Sensors in Active Structural Acoustic Approaches," *Journal of the Acoustic Society of America*, 91(6), pp. 3321-3329, 1992.

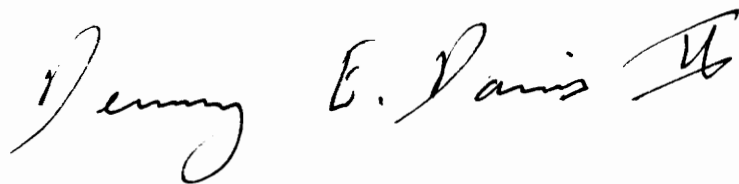
[36] J.S. Arora, *Introduction to Optimum Design*, McGraw Hill, New York, New York, 1989.

[37] K. Schittkowschi, "NLPQL: A FORTRAN Subroutine Solving Constrained Non-linear Programming Problems," *Annals of Operations Research*,, Vol. 5, pp.485-500, 1989.

[38] Kinsler and Frey, *Fundamentals of Acoustics*, John Wiley & Sons, Inc., New York, 1982.

Vita

Denny Earl Davis II was born October 4, 1967 in Radford Virginia. He lived most of his life in the once small town of Fredericksburg Virginia, which is surrounded by Spotsylvania County. This is an area rich in the history of the Civil War. Beginning a college career at Virginia Tech in 1986, he became interested in perusing a graduate degree while working on an independent study with Dr. Craig Rogers in the areas of composites, smart materials, modal analysis and acoustics. He began graduate school immediately upon graduating with a B.S. in Mechanical Engineering in May of 1991. Upon completion of his M.S. also in Mechanical Engineering, he has accepted employment with the research division at the Covington mill of Westvaco.

A handwritten signature in black ink that reads "Denny E. Davis II". The signature is written in a cursive style with a large, stylized initial 'D' and a flourish at the end.